The Astrophysical Journal, 836:38 (18pp), 2017 February 10 https://doi.org/10.3847/1538-4357/836/1/38

Galaxy–Galaxy Weak-lensing Measurements from SDSS. I. Image Processing and Lensing Signals

Wentao Luo[1,2,3], Xiaohu Yang[3,4], Jun Zhang[3], Dylan Tweed[3], Liping Fu[5], H. J. Mo[6,7], Frank C. van den Bosch[8], Chenggang Shu[5], Ran Li[9], Nan Li[10,11,12], Xiangkun Liu[13], Chuzhong Pan[13], Yiran Wang[14], and Mario Radovich[15,16]
[1] Key Laboratory for Research in Galaxies and Cosmology, Shanghai Astronomical Observatory, Nandan Road 80, Shanghai 200030, China; walt@shao.ac.cn
[2] Center for Astronomy and Astrophysics, Shanghai Jiaotong University, Shanghai, 200240, China; xyang@sjtu.edu.cn
[3] Department of Physics, Carnegie Mellon University, Pittsburgh, PA 15213, USA
[4] IFSA Collaborative Innovation Center, Shanghai Jiao Tong University, Shanghai 200240, China
[5] Shanghai Key Lab for Astrophysics, Shanghai Normal University, 100 Guilin Road, 200234, Shanghai, China
[6] Department of Astronomy, University of Massachusetts, Amherst, MA 01003-9305, USA
[7] Physics Department and Center for Astrophysics, Tsinghua University, Beijing 10084, China
[8] Department of Astronomy, Yale University, P.O. Box 208101, New Haven, CT 06520-8101, USA
[9] Key Laboratory for Computational Astrophysics, Partner Group of the Max Planck Institute for Astrophysics, National Astronomical Observatories, Chinese Academy of Sciences, Beijing, 100012, China
[10] Department of Astronomy & Astrophysics, The University of Chicago, 5640 South Ellis Avenue, Chicago, IL 60637, USA
[11] Argonne National Laboratory, 9700 South Cass Avenue B109, Lemont, IL 60439, USA
[12] Kavli Institute for Cosmological Physics at the University of Chicago, Chicago, IL 60637, USA
[13] Department of Astronomy, Peking University, Beijing 100871, China
[14] Department of Astronomy, University of Illinois at Urbana-Champaign, 1002 W. Green Street, Urbana, IL 61801, USA
[15] INAF-Osservatorio Astronomico di Napoli, via Moiariello 16, I-80131 Napoli, Italy
[16] INAF-Osservatorio Astronomico di Padova, vicolo dell'Osservatorio 5, I-35122 Padova, Italy
Received 2016 July 18; revised 2016 December 1; accepted 2017 January 4; published 2017 February 7

Abstract

We present our image processing pipeline that corrects the systematics introduced by the point-spread function (PSF). Using this pipeline, we processed Sloan Digital Sky Survey (SDSS) DR7 imaging data in r band and generated a galaxy catalog containing the shape information. Based on our shape measurements of the galaxy images from SDSS DR7, we extract the galaxy–galaxy (GG) lensing signals around foreground spectroscopic galaxies binned in different luminosities and stellar masses. We estimated the systematics, e.g., selection bias, PSF reconstruction bias, PSF dilution bias, shear responsivity bias, and noise rectification bias, which in total is between -9.1% and 20.8% at 2σ levels. The overall GG lensing signals we measured are in good agreement with Mandelbaum et al. The reduced χ^2 between the two measurements in different luminosity bins are from 0.43 to 0.83. Larger reduced χ^2 from 0.60 to 1.87 are seen for different stellar mass bins, which is mainly caused by the different stellar mass estimator. The results in this paper with higher signal-to-noise ratio are due to the larger survey area than SDSS DR4, confirming that more luminous/massive galaxies bear stronger GG lensing signals. We divide the foreground galaxies into red/blue and star-forming/quenched subsamples and measure their GG lensing signals. We find that, at a specific stellar mass/luminosity, the red/quenched galaxies have stronger GG lensing signals than their counterparts, especially at large radii. These GG lensing signals can be used to probe the galaxy–halo mass relations and their environmental dependences in the halo occupation or conditional luminosity function framework.

Key words: galaxies: clusters: general – gravitational lensing: weak – techniques: image processing

1. Introduction

The nature of dark matter remains a mystery in the current paradigm of structure formation (see Bertone et al. 2005, for a review). Although many experiments have been proposed to directly detect signatures of dark matter, such as particle annihilation, particle decay, and interaction with other particles (see Feng 2010, for a review), the main avenue to probe the existence and properties of dark matter is still through the gravitational potentials associated with the structures in the dark matter distribution.

One promising way to detect the gravitational effects of dark matter structures is through their gravitational lensing effect, in which light rays from distant sources are bent by foreground massive objects such as galaxies or clusters of galaxies residing in massive dark matter halos. In the case of galaxies, the multiple images prediction was first observationally confirmed by Walsh et al. (1979). Since then, more and more strong-lensing systems have been found and analyzed (e.g., Oguri et al. 2002; Kneib et al. 2004; Broadhurst et al. 2005; Treu et al. 2006; Cabanac et al. 2007; Bolton et al. 2008; Coe et al. 2013). In addition, smaller distortions in galaxy images have been detected in large surveys, such as the Sloan Digital Sky Survey (SDSS), Canada–France–Hawaii Telescope Legacy Survey (CFHTLS), and Subaru weak-lensing survey. These are referred to as weak-lensing effects and have been studied very extensively in the past decade (Kaiser et al. 1995; Sheldon et al. 2004; Mandelbaum et al. 2005, 2006; Wittman et al. 2006; Fu et al. 2008; Bernstein 2009; Cacciato et al. 2009; Oguri et al. 2009; George et al. 2012; Kilbinger et al. 2013; Li et al. 2013; Mandelbaum et al. 2013; Li et al. 2014).

Weak gravitational lensing studies are further subdivided into two categories: lensing effects based on individual massive systems, such as clusters of galaxies, and galaxy–galaxy (GG) lensing, which relies on the stacking of lensing signals around many galaxies. For deep surveys such as CFHTLenS (Heymans et al. 2012), DES (Jarvis et al. 2015), DLS (Wittman et al. 2006),

EUCLID (Refregier et al. 2010), LSST (LSST Science Collaboration et al. 2009), KIDS (Kuijken et al. 2015), and the Subaru weak-lensing survey (Kaifu 1998; Umetsu et al. 2007), the number density of background galaxies around a single cluster is sufficient to measure the weak-lensing signals with high signal-to-noise ratio (S/N), so that the mass and shape of the dark matter distribution can be obtained (Oguri et al. 2010). For shallower surveys and for less massive systems, such as SDSS (York et al. 2000), stacking lensing signals around many systems is the only way to measure the weak-lensing effects with sufficient S/N. Although unable to give dark matter distributions associated with individual systems, GG lensing provides a powerful tool to estimate the average mass and profile of dark matter halos around galaxies with certain properties, such as luminosity, stellar mass, etc.

In principle, weak gravitational lensing can provide a clean measurement of the total mass distribution of the lens system. However, the lensing signals are weak, and a number of effects need to be understood and modeled accurately to obtain reliable results. These include uncertainties in photometric redshifts, intrinsic alignment, source selection bias, and mask effect (Yang et al. 2003; Mandelbaum et al. 2005, 2006; Yang et al. 2006a, 2006b; Mandelbaum et al. 2008, 2009a, 2009b; Li et al. 2009; Sheldon et al. 2009; Liu et al. 2015). In addition, accurate image measurements are absolutely essential in GG lensing studies. Thus, for any weak-lensing survey, an image processing pipeline has to be developed first and validated by a series of test simulations, such as STEP (Shear TEsting Program; Heymans et al. 2006; Massey et al. 2007b), GREAT08 (Bridle et al. 2009), GREAT10 (Kitching et al. 2010), GREAT3 (Mandelbaum et al. 2014), and Kaggle—the dark matter mapping competition.[17] Other independent software, such as SHERA (Mandelbaum et al. 2012, hereafter M12), have also been designed for specific surveys.

Many groups have developed image processing pipelines devoted to improving the accuracy of shape measurements for weak-lensing studies (Kaiser et al. 1995; Bertin & Arnouts 1996; Maoli et al. 2000; Rhodes et al. 2000; van Waerbeke 2001; Bernstein & Jarvis 2002; Bridle et al. 2002, p. 38; Bacon & Taylor 2003; Hirata & Seljak 2003; Refregier 2003; Heymans et al. 2005; Zhang 2010, 2011; Bernstein & Armstrong 2014; Zhang et al. 2015). Among these, Lensfit (Miller et al. 2007, 2013; Kitching et al. 2008) applies a Bayesian-based model-fitting approach, the BFD (Bayesian Fourier domain) method (Bernstein & Armstrong 2014) carries out Bayesian analysis in the Fourier domain, using the distribution of unlensed galaxy moments as a prior, and the Fourier_Quad method developed by (Zhang 2010, 2011; Zhang et al. 2015; Zhang 2016) uses image moments in the Fourier domain.

In this paper we attempt to develop an image processing pipeline for weak-lensing studies by combining the Bernstein & Jarvis (2002, hereafter BJ02) method (see Appendix A for details) with the re-Gaussianization method introduced in Hirata & Seljak (2003, hereafter HS03). We test the performance of our pipeline using a number of commonly adopted simulations, and we apply our method to the SDSS data. The structure of the paper is as follows. In Section 2, we describe the procedures used to construct our image processing pipeline. The pipeline is tested using simulations in Section 3. Section 4 presents the SDSS DR7 data used for our investigation. In Section 5, we provide some tests on the systematic errors associated with the GG lensing measurements. Our GG lensing results obtained for galaxies of different luminosities and colors are presented in Section 6. Finally, we summarize our results in Section 7. In addition, some details of our method are given in Appendix A, and our main results for the SDSS data are listed in tables presented in Appendix B. All the GG lensing data shown in this paper can be downloaded from http://gax.shao.ac.cn/wtluo/weak_lensing/wl_sdss_dr7.tar.gz.

[17] Supported by NASA and the Royal Astronomical Society.

2. Image Processing Pipeline

The goal of our pipeline is to measure, for each observed galaxy image $I_{\rm obs}(\boldsymbol{x})$, two ellipticity parameters e_1 and e_2 (to be defined below) that describe the intrinsic shape of the galaxy. However, the observed image is the convolution between the intrinsic galaxy image $I_{\rm int}(\boldsymbol{x})$ and the point-spread function (PSF) $P(\boldsymbol{x})$,

$$I_{\rm obs}(\boldsymbol{x}) = I_{\rm int}(\boldsymbol{x}) \otimes P(\boldsymbol{x}), \quad (1)$$

where $I_{\rm int}(\boldsymbol{x})$ stands for the intrinsic galaxy surface brightness and $P(\boldsymbol{x})$ is the PSF. Formally, the impact of the PSF on the ellipticity parameters can be written as

$$e_i^{\rm obs} = (1+m)e_i^{\rm int} + c, \quad (2)$$

where $i = 1, 2$. PSF anisotropy causes a nonzero additive error c, while PSF smearing causes a nonzero multiplicative error m. The challenge is to develop a reduction pipeline that minimizes both $|m|$ and $|c|$. Our pipeline consists of the following steps:

1. Create a kernel function $K(\boldsymbol{x})$to correct for the PSF anisotropy (see Section 2.1 for details).
2. Convolve both $I_{\rm obs}(\boldsymbol{x})$ and $P(\boldsymbol{x})$ with the kernel function $K(x)$, so that we have $I_1(\boldsymbol{x}) = I_{\rm obs}(\boldsymbol{x}) \otimes K(\boldsymbol{x})$ and $P_1(\boldsymbol{x}) = P(\boldsymbol{x}) \otimes K(\boldsymbol{x})$.
3. Measure the sizes T_I and T_P, as well as the ellipticity parameters e_1 and e_2, from the surface-brightness-weighted second moments of I_1 and P_1, M_{I_1} and M_{P_1}, respectively, using the adaptive Gaussian kernel method as described in Section 2.2.
4. Re-Gaussianize P_1 and I_1 using the method of HS03. This results in $P_{\rm RG} = G(M_{P_1})$ and $I_{\rm RG} = I_1 - G(M_{I_1}) \otimes [P_1 - G(M_{P_1})]$. Here $G(M_{P_1})$ and $G(M_{I_1})$ are 2D Gaussian functions reconstructed from the same second moments M_{P_1} and M_{I_1} obtained from P_1 and I_1.
5. Expand $I_{\rm RG}$ and $P_{\rm RG}$ in terms of the quantum harmonic oscillator (QHO) eigenfunctions, as described in Section 2.1. Compute $\beta_{22}^I = b_{22}^I/b_{00}^I$ and $\beta_{22}^P = b_{22}^P/b_{00}^P$, where b_{ij}^I and b_{ij}^P are the coefficients of the QHO expansions of $I_{\rm RG}$ and $P_{\rm RG}$, respectively.
6. Calculate the resolution factor $\mathcal{R}$, which is defined as

$$\mathcal{R} = 1 - \frac{T_P(1-\beta_{22}^p)/(1+\beta_{22}^p)}{T_I(1-\beta_{22}^I)/(1+\beta_{22}^I)}, \quad (3)$$

and correct the ellipticity parameters according to $e_1^{\rm corr} = e_1/\mathcal{R}$ and $e_2^{\rm corr} = e_2/\mathcal{R}$.
7. Rotate $(e_1^{\rm corr}, e_2^{\rm corr})$, which are measured with respect to the coordinates of the CCD image (i.e., e_1 is measured in the direction of CCD pixel rows), such that e_1 is aligned with the direction of increasing R.A. This is achieved by

the transformation

$$\begin{pmatrix} e_1^{\rm rot} \\ e_2^{\rm rot} \end{pmatrix} = \begin{pmatrix} \cos 2\phi & -\sin 2\phi \\ \sin 2\phi & \cos 2\phi \end{pmatrix} \begin{pmatrix} e_1^{\rm corr} \\ e_2^{\rm corr} \end{pmatrix}, \quad (4)$$

where ϕ is the angle between the north and the direction of the CCD columns, and is provided in the header of each CCD image.

8. Background noise of each galaxy is estimated from both the sky and the dark current as in Mandelbaum et al. (2005, hereafter M05),

$$\sigma_{\rm sky} = \frac{\sigma^I}{\mathcal{R}F}\sqrt{4\pi n}, \quad (5)$$

where σ^I is the size of the galaxy in pixels, F is the flux, and n is the sky and dark current brightness in photons per pixel.

The end result of our pipeline is a catalog listing for each source image the values of $e_1^{\rm rot}$, $e_2^{\rm rot}$, $\mathcal{R}$, $\sigma_{\rm sky}$, α, δ, and $z_{\rm photo}$, where α, δ, and $z_{\rm photo}$ are the R.A., decl., and photometric redshift of the source (galaxy), respectively. Note that we explicitly list $\mathcal{R}$ since it is a common practice in GG lensing measurements to only select images with $\mathcal{R}$ exceeding some limiting value. Throughout this paper we follow M05 and only use images with $\mathcal{R} > 1/3$.

2.1. PSF Anisotropy Correction

There are two systematics associated with the PSF. One is an isotropic smearing of the original image, and the other is an anisotropic effect that introduces extra shape distortion. Our image processing pipeline is designed to correct for both effects. More specifically, we use the rounding kernel method of BJ02 for the anisotropic correction and the re-Gaussianization method of HS03 for the isotropic correction. The reason for this combination is that, according to our test with STEP2 data, the multiplicative error it produces is the smallest among the other methods (e.g., BJ02 method alone, re-Gaussianization method alone, and the KSB method). In this subsection, we focus on the PSF anisotropy correction.

The basic idea of the rounding kernel method of BJ02 for PSF anisotropy corrections is to convolve the PSF with a reconstructed kernel. In the ideal case, the Fourier transformation of the kernel K is related to the PSF as $\tilde{K} = 1/\tilde{P}$, so that the convolution of K and P in real space is a delta function. In that case we have

$$K(\boldsymbol{x}) \otimes P(\boldsymbol{x}) = \delta(\boldsymbol{x}) \quad (6)$$

and

$$I_{\rm int}(\boldsymbol{x}) = I_{\rm obs}(\boldsymbol{x}) \otimes K(\boldsymbol{x}), \quad (7)$$

where $I_{\rm obs}$ is the observed image, $I_{\rm int}$ is the intrinsic image, and $K(\boldsymbol{x})$ represents the reconstructed kernel (see Equations (7.1)–(7.4) in BJ02). In real applications, the PSF is not modeled perfectly; a better kernel approximation is needed to serve our purpose. To this end, we expand the PSF with the QHO eigenfunctions,

$$P = \sum_{p,q} b_{pq}\phi_{pq}^{\sigma}(r, \theta), \quad (8)$$

and write its convolution with K as

$$K \otimes P = \sum_{p,q} b_{pq}^{*}\phi_{pq}^{\sigma}(r, \theta), \quad (9)$$

where

$$\phi_{pq}^{\sigma}(r, \theta) = \frac{(-1)^q}{\sqrt{\pi}\sigma^2}\sqrt{\frac{q!}{p!}}(r/\sigma)^m e^{im\theta}e^{-r^2/2\sigma^2}L_q^m(r^2/\sigma^2). \quad (10)$$

L_q^m are the Laguerre polynomials obeying $m = p - q$, and σ is the size of the object in pixel units. If b_{pq}^{*} satisfies

$$b_{pq}^{*} = [(-1)^p/\sqrt{\pi}]\delta_{pq} \quad (11)$$

up to some order $N = p + q$, the PSF anisotropy is then ideally removed by the reconstructed kernel. Note that b_{10}^{*} can be set to 0 if the PSF centroid is properly measured, and the dominant bias is introduced by b_{20}^{*}, b_{31}^{*}, and so on (see Appendix A for details).

2.2. Shape Parameters

In this subsection, we outline a few parameters that are important in GG lensing shear measurements, as well as in our image processing pipeline. The shape parameters, e_1 and e_2, are obtained from the surface-brightness-weighted second moment of the 2D galaxy image (Kaiser et al. 1995; Bartelmann & Schneider 2001),

$$M_{ij} = \frac{\sum G(\boldsymbol{x})I(\boldsymbol{x})(\boldsymbol{x} - \boldsymbol{x}_0)_i(\boldsymbol{x} - \boldsymbol{x}_0)_j}{\sum G(\boldsymbol{x})I(\boldsymbol{x})}, \quad (12)$$

where $i, j = x, y$ and $I(\boldsymbol{x})$is the surface brightness at the pixel located at $\boldsymbol{x}$. The function $G(\boldsymbol{x})$is an adaptive Gaussian kernel (see Section 2.1 in HS03) used to avoid divergent noise (Kaiser et al. 1995):

$$G(\boldsymbol{x}) = \exp[-0.5 * (\boldsymbol{x} - \boldsymbol{x}_0)^{\rm T}M^{-1}(\boldsymbol{x} - \boldsymbol{x}_0)], \quad (13)$$

with $\boldsymbol{x}_0$ being the centroid vector,

$$\boldsymbol{x}_0 = \frac{\int \boldsymbol{x}G(\boldsymbol{x})I(\boldsymbol{x})d^2\boldsymbol{x}}{\int G(\boldsymbol{x})I(\boldsymbol{x})d^2\boldsymbol{x}}. \quad (14)$$

Following convention, the ellipticity parameters e_1 and e_2 are respectively defined as the compressions along a fiducial direction (e.g., x) and along a direction rotated 45° with respect to it. The size T is defined as the trace of the moment tensor. Thus,

$$\begin{aligned} e_1 &= \frac{M_{xx} - M_{yy}}{M_{xx} + M_{yy}} \\ e_2 &= \frac{2M_{xy}}{M_{xx} + M_{yy}} \\ T &= M_{xx} + M_{yy}. \end{aligned} \quad (15)$$

2.3. Re-Gaussianization

The PSF isotropic effect, aka smearing effect, dilutes the value of ellipticity and therefore leads to shear underestimation. The method we adopt here to correct this effect is the re-Gaussianization method from HS03. It consists of applying a resolution factor $\mathcal{R}$ (Equation (3)) to correct for the ellipticity parameters. Note, however, as pointed out in HS03, that

Equation (3) (Equation (14) in HS03) is only valid when both PSF and galaxy images are Gaussian, which does not apply to real observations. HS03 reconstructed a Gaussian PSF model using the second moments from the PSF and then corrected the galaxy image for the effect of the residuals. We assume that Equation (3) is valid after these treatments. The related processes are called re-Gaussianization and carried out as follows.

We first construct a Gaussian PSF from the real PSF $P(\boldsymbol{x})$ using the second-moment covariance matrix M_P,

$$G(\boldsymbol{x}) = \frac{1}{2\pi\sqrt{\det M_P}} \exp\left(-\frac{1}{2}\boldsymbol{x}^{\mathrm{T}} M_P^{-1}\boldsymbol{x}\right), \tag{16}$$

with the residual being

$$\epsilon(\boldsymbol{x}) = P(\boldsymbol{x}) - G(\boldsymbol{x}). \tag{17}$$

The galaxy image $I_{\mathrm{obs}}(\boldsymbol{x})$ then satisfies

$$I_{\mathrm{obs}}(\boldsymbol{x}) = P(\boldsymbol{x}) \otimes I_{\mathrm{int}}(\boldsymbol{x}) = G(\boldsymbol{x}) \otimes I_{\mathrm{int}}(\boldsymbol{x}) + \epsilon(\boldsymbol{x}) \otimes I_{\mathrm{int}}(\boldsymbol{x}), \tag{18}$$

where $I_{\mathrm{int}}(\boldsymbol{x})$ is the intrinsic brightness distribution of the galaxy.

Next, we approximate the galaxy image also with a Gaussian distribution from its second-moment matrix, M_I',

$$I_{\mathrm{obs}}^0(\boldsymbol{x}) = \frac{1}{2\pi\sqrt{\det M_I'}} \exp\left(-\frac{1}{2}\boldsymbol{x}^{\mathrm{T}} M_I'^{-1}\boldsymbol{x}\right), \tag{19}$$

where $M_I' = M_I - M_P$ denotes the galaxy second-moment matrix once the PSF contribution has been subtracted.

Finally, an image, corrected for the residual between real PSF and Gaussian PSF, is obtained using

$$I_{\mathrm{obs}}'(\boldsymbol{x}) = I_{\mathrm{obs}}(\boldsymbol{x}) - \epsilon(\boldsymbol{x}) \otimes I_{\mathrm{obs}}^0(\boldsymbol{x}). \tag{20}$$

In our pipeline, we compute the β_{22} from $I_{\mathrm{obs}}'(\boldsymbol{x})$ and $G(\boldsymbol{x})$.

2.4. Shear Estimator

Once we have processed all the source images, we can obtain the shear signals γ along any desired directions. We first compute the responsiveness $\bar{R}$ of our survey galaxies, which is defined as

$$\bar{R} \equiv 1 - \frac{1}{N}\sum_{i=1}^{N}(e_1^{\mathrm{rot}})^2, \tag{21}$$

where N is the total number of source images with $\mathcal{R} > 1/3$. Next, we compute the shear components γ_1 and γ_2 using all the images sampling the local shear field:

$$\gamma_l = \frac{1}{2\bar{R}}\frac{\sum w_i e_l^{\mathrm{rot}}}{\sum w_i}, \tag{22}$$

where $l = 1, 2$ and w_i is a weighting function. Each source image is weighted by

$$w = \frac{1}{\sigma_{\mathrm{sky}}^2 + \sigma_{\mathrm{shape}}^2}, \tag{23}$$

where σ_{sky} is the background noise estimated using Equation (5) and σ_{shape} is the shape noise. For a sample of background galaxies, the shape noise is defined as the variance of their ellipticities.

Observationally, the tangential shear γ_{T} as a function of radius around foreground lens galaxies is estimated as

$$\gamma_{\mathrm{T}}(R) = \frac{1}{2\bar{R}}\frac{\sum w_i e_{\mathrm{T}}}{\sum w_i}, \tag{24}$$

where e_{T} is given by

$$\begin{pmatrix} e_{\mathrm{T}} \\ e_{45^0} \end{pmatrix} = \begin{pmatrix} \cos 2\theta & -\sin 2\theta \\ \sin 2\theta & \cos 2\theta \end{pmatrix}\begin{pmatrix} e_1^{\mathrm{rot}} \\ e_2^{\mathrm{rot}} \end{pmatrix}, \tag{25}$$

with θ the angle between the line connecting the lens and the source and the direction of increasing R.A. So defined, e_{T} is the shape parameter along the tangential direction around the lens.

3. Testing the Pipeline with Simulations

Before applying our pipeline to real data, we benchmark test it using simulated images. These contain input shear signals, as well as observational effects, such as PSF, sky background noise, and pixelization. The two simulation catalogs used here are SHERA (SHEar Reconvolution Analysis; developed by M12) and GREAT3 (as described in Mandelbaum et al. 2014).

3.1. Testing with SHERA

3.1.1. SHERA Data

SHERA (M12) is designed to test the accuracy of shape measurement pipelines for ground-based images. It uses Cosmological Evolution Survey (COSMOS) images as input. The output are low-resolution images expected from a given ground-based observation. Parameters such as pixel size, PSF size, and sky background are set in accordance to SDSS data. The weak-lensing shear signal is added to each image using the following equation:

$$\begin{pmatrix} x^u \\ y^u \end{pmatrix} = \begin{pmatrix} 1-\kappa-\gamma_1 & -\gamma_2 \\ -\gamma_2 & 1-\kappa+\gamma_1 \end{pmatrix}\begin{pmatrix} x^l \\ y^l \end{pmatrix}, \tag{26}$$

where (x^u, y^u) are the unlensed coordinates and (x^l, y^l) the lensed ones. The input shear (γ_1, γ_2) are randomly generated, ranging from -0.05 to 0.05.

The input galaxy image catalog is constructed from the COSMOS ACS field (Koekemoer et al. 2007; Scoville et al. 2007a, 2007b) following the method described in Leauthaud et al. (2007). The survey field is a 1.64 square degree region centered at 10:00:28.6, +0.12:12:21.0 (J2000). The images are corrected for charge transfer inefficiency (Massey et al. 2010, CTI), geometric distortion, sky subtraction, and cosmic rays and are further dithered using the multidrizzle algorithm. The final production is a co-added image of 7000×7000 pixels with a scale of $0\farcs03$ pixel^{-1}. Further cuts are applied to fulfill the special requirements of SHERA, as described in Section 4.1 of M12.

With the above criteria, 30,225 galaxies are selected. To mimic the SDSS images, additional galaxies are discarded either because these sources are undetectable in SDSS or because their sizes are smaller than the SDSS PSF, as detailed in M12. The final sample contains 26,113 galaxies.

3.1.2. PSF Matching

The high-resolution images obtained above are transformed into low-resolution ones by PSF matching, i.e., by first

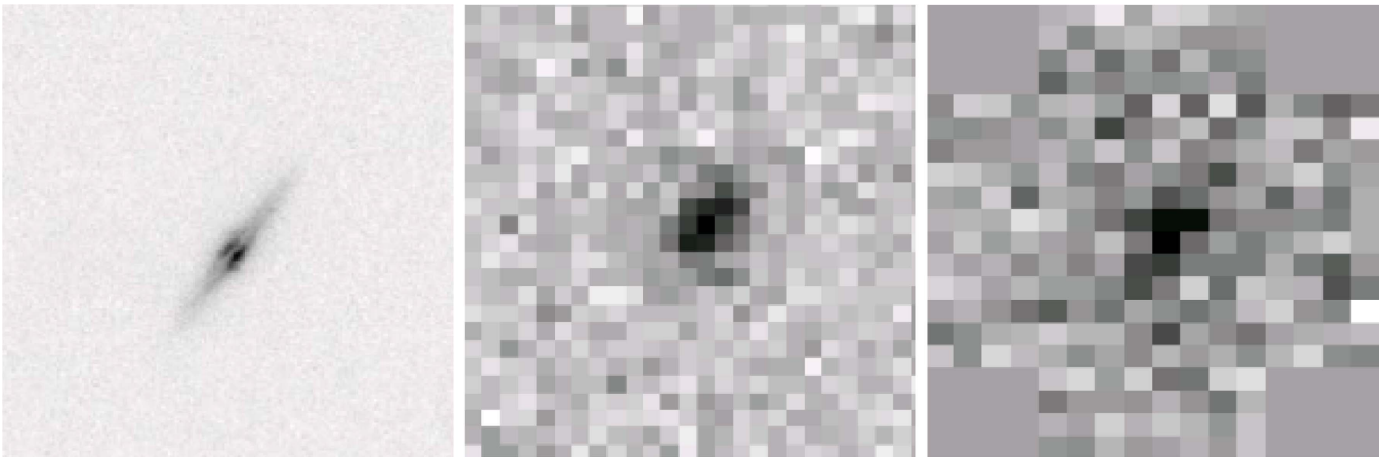

Figure 1. COSMOS image (left panel), SHERA simulated image (middle panel), and SDSS real image of the same galaxy (right panel).

deconvolving the images with the space PSF and then convolving them with the ground-based PSF. In Fourier space, this is mathematically given by

$$\tilde{I}^g = \frac{\tilde{G}^g}{\tilde{G}^s}\tilde{I}^s, \tag{27}$$

where I^g and G^g are the ground-based brightness distribution and PSF, respectively, whereas I^s and G^s are the corresponding space-based quantities. This PSF matching works as long as the power spectrum of the space PSF is larger than that of the ground PSF for all k; otherwise, it leads to a ringing effect in the new image. As shown in Figure 2 of M12, the power spectrum of the SDSS PSF is smaller than that of COSMOS at all wavenumbers, so the PSF matching can be done safely.

In addition to the PSF, the noise level at the position of COSMOS in the SDSS imaging should also be taken into account. Figure 1 shows the COSMOS image of a typical disk galaxy (left), the SHERA simulated SDSS image (middle), and the real SDSS fpAtlas image (right) of the same galaxy. The bulge and disk components can be clearly identified from the original COSMOS image, whereas in SDSS only a small number of pixels brighter than the detection limit (22.0 in r band) can be identified. We downgrade the high-resolution COSMOS images to low-resolution SDSS images. During this process, we miss 2.2% of the objects because of masking, which leaves a total of 25,527 images.

3.1.3. SHERA Testing Results

Using the mock SDSS images obtained above, we follow M12 and rotate each image 90° in order to eliminate the effect from intrinsic galaxy shape. In the spirit of making a fair comparison with the results of M12, the sky background and Poisson noise are not added to the simulation, so as to assess the performance of the PSF correction alone. Due to the size cut, only about 11,700 (44%) galaxies are selected for the final shear measurements.

We measured the two shear components $\gamma_1^{\rm measure}$ and $\gamma_2^{\rm measure}$ and compare them to the input signals in Figure 2. The upper left and lower left panels are the one-to-one correlations for the two components, while the right panels are the corresponding residuals plotted against the input signals. The red lines are the linear fit to the data points. We use the standard terminology of multiplicative error (including the PSF smearing effect and

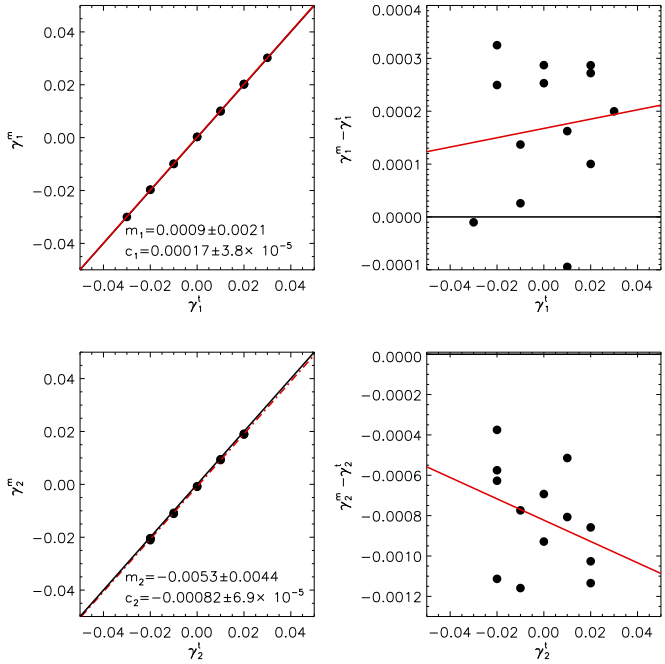

Figure 2. Correlation between the true (input) and measured shear components γ_1 (upper left) and γ_2 (lower left). The corresponding residuals are plotted against the input values in the right panels. The red lines are linear fits.

other unknown biases in the measurement method itself) and additive error (mostly from PSF anisotropy) to relate the input signal and the measured signal:

$$\gamma_i^{\rm measure} = (1 + m_i)\gamma_i^{\rm input} + c_i \quad (i = 1, 2), \tag{28}$$

where m_i and c_i represent the two types of errors. In general, our pipeline achieves <1% in the multiplicative error, with $m_1 = 0.09\% \pm 0.0021$ and $m_2 = 0.53\% \pm 0.0044$, and <0.1% in the additive error, with $c_1 = 0.00017 \pm 3.8 \times 10^{-5}$ and $c_2 = 0.00082 \pm 6.9 \times 10^{-5}$. The fact that the multiplicative error in γ_2 is larger than the one in γ_1 is due to pixelization. In Mandelbaum et al. (2012) the corresponding multiplicative errors are $m_1 = -1.6\% \pm 0.001$ and $m_2 = -2.7\% \pm 0.001$, and the additive errors are $c_1 = 0.00028 \pm 1.0 \times 10^{-5}$ and $c_2 = -0.00011 \pm 1.0 \times 10^{-5}$. These values demonstrate that the performances of the two pipelines are favorably comparable.

However, some shortcomings of our pipeline appear during our tests. When strong sky background and Poisson noise are added, our pipeline sometimes suffers from nonconvergence either during the calculation of the adaptive moments or during the estimation of the coefficients (see Equation (42) in Appendix A). Thus, our pipeline cannot provide shape measurements for images with too low qualities. This reduces the number of sources that can be used for lensing studies. Due to the fact that the COSMOS image sample is small, we do not perform further tests with noise as in M12. The convergence problem is also not discussed further, because it is difficult to determine whether it is caused by the iteration of adaptive moments or by the procedure constraining the k_{ij} (see Appendix A). Nevertheless, as we will show in the next subsection, even with the reduced number of sources, our pipeline provides lensing signals that are competitive with other methods or implementations.

3.2. GREAT3

GREAT3 (Mandelbaum et al. 2014) is the continuation of the testing projects STEP (Heymans et al. 2005), STEP2 (Massey et al. 2007b), GREAT08 (Bridle et al. 2009), and GREAT10 (Kitching et al. 2010). All of these code comparison projects are designed to compare the performances of different shape measurement methods in different observational conditions. From STEP to GREAT3, different PSFs, pixel sizes, and galaxy morphologies are adopted. In particular, GREAT3 uses controlled galaxy morphologies generated with Shapeless (Refregier 2003), real galaxy morphologies obtained from COSMOS, co-added multiply observed images, variable PSF, and variable shears. Five major branches of simulations are generated using GalSim (Rowe et al. 2015): (i) a controlled sample generated with parametric (single or double Sérsic) galaxy models; (ii) a real galaxy sample with realistic morphology from the *Hubble Space Telescope* COMOS data set; (iii) a multiple-epoch sample containing six images combined by dithering; (iv) a sample with variable PSF that is reconstructed from star images; (v) a sample that includes all the above procedures. Each major branch is further divided into ground versus space and constant versus variable shear sub-branches.

For the constant shear data sets, 10,000 galaxies with shear are simulated. In order to cancel the effect of galaxy intrinsic shape, GREAT3 applies the same rotation method as in the STEP2 simulation (Massey et al. 2007b). The basic idea is to use the fact that the shape is a spin-two quantity, meaning that the sum of the original and 90° rotated ellipticity is zero.

Our pipeline participated in the controlled ground constant, the controlled space constant, the real ground constant, and the real space constant tests. We labeled our implementation as BJ02+HS03 within this project. Overall, it ranks 15 among a total of 26 participating pipelines. As mentioned earlier, our pipeline suffers from the convergence problem. Together with the size cut using the resolution factor in Equation (3), only about 40% of galaxies are used in the competition. Among our submissions, we found that the best weighting scheme for our pipeline was to take the inverse of the shape noise and errors from ellipticity as in Mandelbaum et al. (2015, hereafter M15).

Our testing results in GREAT3 are not very good, which is mainly caused by the high failure rate of our image processing pipeline. As only about 40% of galaxies are used in our competition, our pipeline does not benefit much from the 90° rotation, which was supposed to cancel intrinsic shape noise. The small number of remaining sources in our competition thus results in quite big selection errors. For instance, in the Real Ground Constant branch, the multiplicative bias is ∼7%. Within the error budget, the noise-induced bias estimated using Equation (34) is 0.35% at most, given a median resolution factor of 0.41 and setting $S/N = 20$ for all the galaxies. The remaining is thus mostly the selection bias. Quite interestingly, as we have tested, if we set pixel values in the GREAT3 images that are below 1σ sky level to be zero, it can partly alleviate our convergence problem. However, due to the time limit, we were not able to carry out more detailed tests in GREAT3. The more detailed information and results about the GREAT3 competition can be found in M15.

4. The Source and Lens Galaxies in SDSS DR7

Since our pipeline proved to be reliable, we processed the SDSS DR7 (Abazajian et al. 2009) *r*-band imaging data. SDSS (York et al. 2000) consists of three imaging and spectroscopic surveys (Legacy, SEGUE, and Supernova), using a 2.5 m telescope at Apache Point Observatory in Southern New Mexico. The SDSS photometric camera has two TDI (Time-Delay-and-Integrate) CCD scanning arrays (Gunn et al. 1998). One is a 6 × 5 CCD array, with each of the CCDs having 2048 × 2048 pixels (24 μm ≈ 3″ on the sky) for five-band photometry, and the other is a 24,2048 × 400 CCD array used for astrometry and focus monitoring. The DR7 imaging data, with *u*, *g*, *r*, *i*, and *z* band, covers about 8423 square degrees of the LEGACY sky (∼230 million distinct photometric objects) and about 3240 square degrees of SEGUE sky (∼127 million distinct objects, including many stars at low latitude). The total number of objects identified as galaxies is around 150 million.

4.1. Source Galaxies

Following Mandelbaum et al. (2005, hereafter M05), we have only chosen galaxies defined as OBJC_TYPE = 3 from the Photo pipeline developed by Lupton et al. (2001). They have to be detected in both *r* and *i* bands (with $r < 22$ and $i < 21.6$ in model magnitudes). We first created a preliminary catalog (referred to hereafter as Cat I) from SDSS casjobs with 115,052,555 galaxies containing positions (including `run`, `rerun`, `camcol`, `field`, `obj`, `ra`, `dec`) and photometric redshifts.

Cat I was then processed to include (i) the sky level in units of photon–electron using the information of gain value in *r* band, (ii) the position of each galaxy in terms of CCD coordinates (in order to get the PSF from psField files), and (iii) the SPA value denoting the angle between the camera column position and the north from fpC files. We refer to this catalog as Cat II; it contains 91,941,657 galaxies. A total of 23,110,898 objects have been discarded from Cat I either because they contain no assigned (value −9999) zero-point extinction coefficient, airmass, or sky in *r* band or because they are not flagged as BINNED1 (detected at ⩾5), SATURATED = 0 (do not have saturated pixels), EDGE = 0 (do not locate at the edge of the CCD), MAYBE-CR = 0 (not cosmic rays), MAYBE-EGHOST = 0 (not electronic ghost line), and PEAKCENTER = 0 (centroiding algorithm works well for this object).

This pipeline was then used to process the images from fpAtlas and psField files in order to generate our final catalog Cat III. Cat III contains the positions, redshift, ellipticity,

Table 1
Properties of the Six Lens Samples Created for This Paper

Sample	M_r	$N_{\rm gal}$	N_{M05}	$\langle z\rangle$	$\sigma(z)$	$\langle L\rangle/L_*$
L1	(−18, −17]	18,614	6524	0.029	0.007	0.071
L2	(−19, −18]	47,795	19,192	0.044	0.012	0.181
L3	(−20, −19]	138,988	58,848	0.069	0.020	0.450
L4	(−21, −20]	249,906	104,752	0.103	0.030	1.082
L5	(−22, −21]	164,653	63,794	0.140	0.038	2.364
L6	(−23, −22]	11,453	6499	0.150	0.037	5.146

Note. We indicate the number of galaxies in the equivalent samples in Mandelbaum et al. (2005) as N_{M05}, to be compared to our number $N_{\rm gal}$.

resolution factor, and calibration errors of each galaxy. The errors have been estimated from both sky background and photon noise as described by Equations (11) and (12) in M05. Only objects with valid e_1, e_2 resolution factors were kept. As mentioned above, our pipeline will discard galaxy images that suffer from the convergence problem during the calculation of ellipticity. From GREAT3 testing, about 40% of galaxies were excluded owing to this effect, and we further require that $\mathcal{R} > 1/3$, which eliminates another 10%–30% (depending on different simulation sets). Cat III has a final number of galaxies of 41,631,361, which is ∼45% of the original Cat II. The irregularity image from the SDSS Photo pipeline (∼4%), resolution cut (∼11%), and nonconvergence (∼40%) together reduce the final catalog by ∼55%.

4.2. Lens Galaxies

We now focus on the lens galaxy sample used for this study. Only galaxies spectroscopically observed in the SDSS DR7 region (Abazajian et al. 2009) have been used here. More specifically, we use the New York University Value-Added Galaxy catalog (Blanton et al. 2005, NYU-VAGC) constructed from SDSS DR7. All galaxies have been extinction corrected, with magnitudes brighter than $r = 17.72$, redshifts within the range $0.01 \leqslant z \leqslant 0.2$, and a spectroscopic redshift completeness $C_z > 0.7$. The completeness C_z is defined as the average percentage of the galaxies that have spectroscopic redshift in their local sky coverage. The resulting galaxy sample contains a total of 639,359 galaxies for a sky coverage of 7748 square degrees.

In the modern galaxy formation paradigm (Mo et al. 2010), brighter/more massive galaxies are believed to reside in higher-mass halos. This suggests that the GG lensing signals should vary with the lens galaxy luminosity or stellar mass. Thus, a sample of brighter or more massive lens galaxies should give a higher lensing signal. This expectation has been proved to be correct in M05, Mandelbaum et al. (2006, hereafter M06), and Sheldon et al. (2009). In M05, lens galaxies in SDSS DR4 are divided into six luminosity samples. We have used the same luminosity binning for our SDSS DR7 galaxies. The selection criteria and galaxy numbers of our six lens galaxy samples are listed in Table 1. The scatter of the redshift distribution, the ratio between the mean luminosity and the characteristic luminosity L_* ($M_* = -20.44$, as given in Blanton et al. 2003), and the number of galaxies contained in each sample are also listed in Table 1. On average, the number of galaxies in our sample is 2 to 3 times larger than the corresponding M05 sample, simply because DR7 covers a larger area than DR4 (7748 versus 4783 square degrees). The mean redshift from our lens sample is slightly lower than that of M05, because M05 also used lenses at $z > 0.2$, while the redshift range of our sample is between 0.01 and 0.2. The redshift distributions of our lens samples are shown in the upper panel of Figure 3. The solid black line is for the total sample, while the colored lines are for the six luminosity samples.

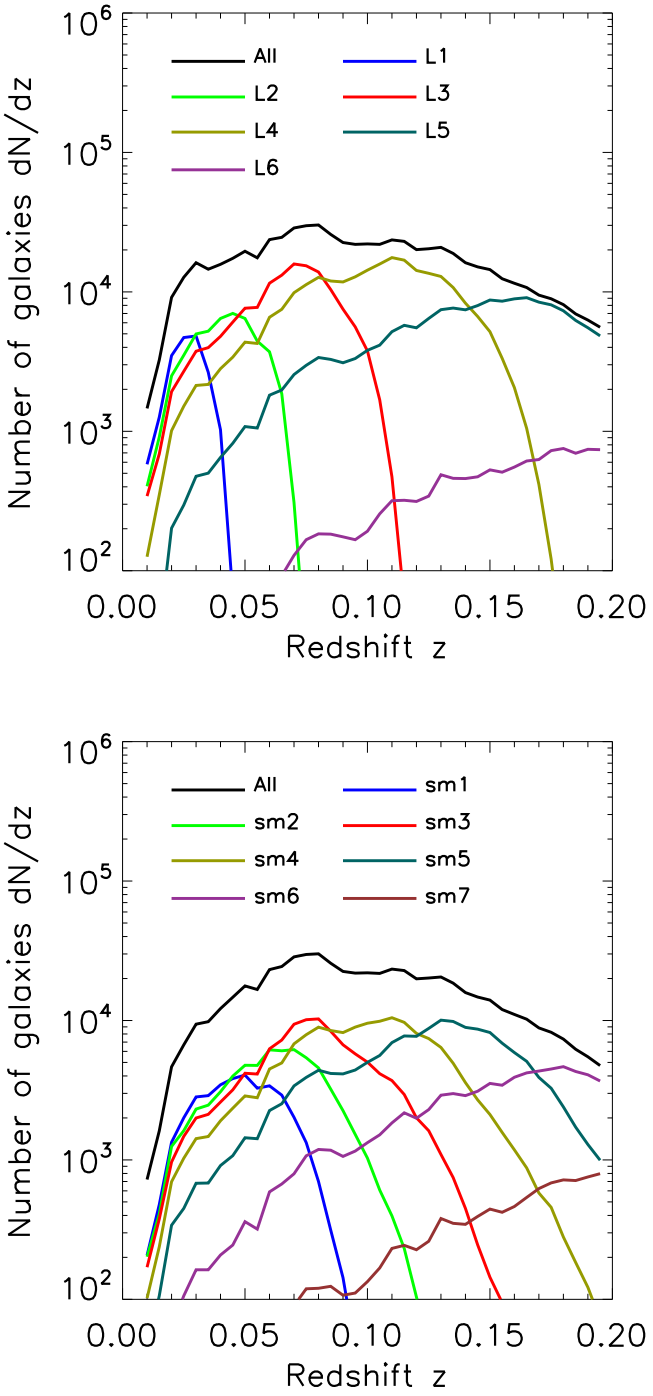

Figure 3. Redshift distribution of lens samples binned in luminosity (upper panel) and in stellar mass (lower panel).

We further divide galaxies in each luminosity bin into blue and red subsamples according to

$$^{0.1}(g - r) = 1.022 - 0.0652x - 0.0031x^2, \qquad (29)$$

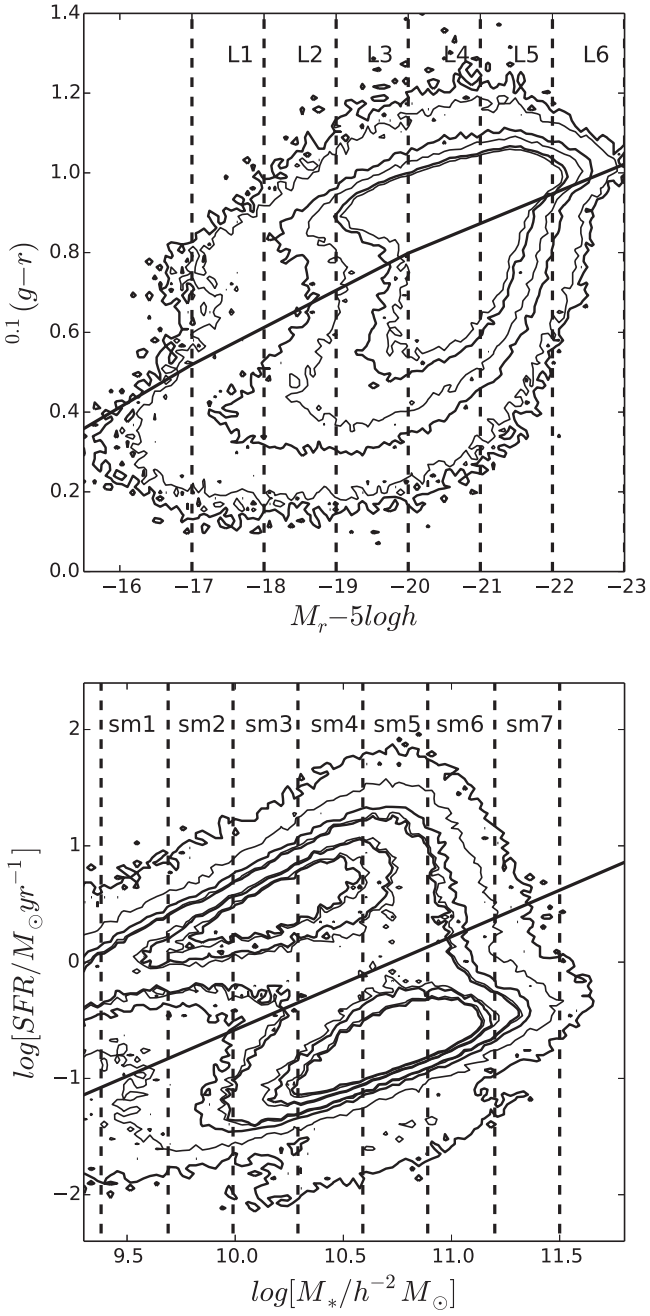

Figure 4. Upper panel: distribution of lens galaxies in the color–absolute magnitude plane, represented by contours. The luminosity bins used in the paper are shown as vertical dashed lines. The solid line is the division between red and blue galaxies adopted from Yang et al. (2008). Lower panel: distribution of lens galaxies in the star formation rate (SFR)–stellar mass plane, represented by contours. The stellar mass bins used in the paper are shown as vertical lines, and the solid line is the separation between star-forming and quenched galaxies adopted from Luo et al. (2014).

where $x = {}^{0.1}M_r - 5\log h + 23.0$ (Yang et al. 2008). The upper panel of Figure 4 shows the distribution of the lens galaxies in the color–absolute magnitude plane, with the black dashed line showing the demarcation line (Equation (29)), and the vertical lines marking the different luminosity bins we use. Table 2 shows the number, mean redshift, scatter in redshift, and mean luminosity in each of the color subsamples.

In M06, GG lensing signals are measured for lens galaxies binned in stellar masses. Here we make a similar binning for our SDSS DR7 galaxies. Note, however, that the stellar masses in M06 are estimated from galaxy spectra, as described in Kauffmann et al. (2003), while the stellar masses in our sample are estimated using the model described in Bell et al. (2003). Table 3 lists the general properties of our samples in different stellar mass bins, such as the number of galaxies in our samples in comparison to that in M06, the mean redshift, the scatter in redshift, and the mean stellar mass. Shown in the lower panel of Figure 3 are the redshift distributions of our lens samples in different stellar mass bins. The solid black line is for the total sample, while the colored lines are for the seven stellar mass samples, as indicated.

Table 2
Properties of the 12 Lens Subsamples Obtained from the One in Table 1 after Being Divided by Color

Sample	$N_{\rm gal}$	$\langle z\rangle$	$\sigma(z)$	$\langle L\rangle/L_*$
L1R	5383	0.030	0.007	0.073
L1B	13,231	0.029	0.007	0.071
L2R	17,471	0.045	0.013	0.186
L2B	30,324	0.044	0.012	0.179
L3R	67,058	0.069	0.019	0.459
L3B	71,930	0.069	0.019	0.443
L4R	138,316	0.102	0.030	1.092
L4B	111,590	0.104	0.030	1.072
L5R	98,808	0.141	0.038	2.378
L5B	65,845	0.138	0.038	2.347
L6R	6880	0.155	0.034	5.130
L6B	4573	0.141	0.037	5.182

We further divide galaxies in each stellar mass bin into red and blue subsamples using Equation (29). Table 4 shows the number, mean redshift, scatter in redshift, and mean stellar mass of the galaxies in each of the color subsamples. In general, the mean stellar mass of the red sample is larger than that for the corresponding blue sample by 0.01–0.02 dex.

In addition to the color separation, we also separate galaxies in different stellar mass bins into star-forming and quenched subsamples. Here we use the scheme given in Yang et al. (2013) and Luo et al. (2014) to define the star-forming and quenched populations, and the dividing line is defined to be

$$\log \mathrm{SFR} = (\log M_* - 2\log h - 11.0) \times 0.8. \quad (30)$$

The lower panel of Figure 4 shows the distribution of galaxies in the SFR–stellar mass plane, with the black line showing the division defined in Equation (30). Note that M_* is presented in units of $h^{-2}\,M_\odot$. Table 5 lists the number, the mean redshift, the scatter in redshift, and the mean stellar mass of each subsample. For each mass bin, the average stellar masses in the two subsamples are similar, while the mean redshifts differ slightly, with the quenched subsample having a slightly higher mean redshift than the corresponding star-forming subsample.

5. Systematic Tests

Before we provide our measurement of the GG lensing signals from SDSS DR7, following M05, we provide a detailed list of possible systematic errors in the measurements. The total possible 2σ systematic error in terms of $\delta\gamma/\gamma$ is about [−9.1%, 20.8%]. This is roughly consistent with those quoted in M05, about [−9.0%, +18.4%], as we are using roughly the same selection criteria for source galaxies. In addition, the redshift tests (using foreground galaxies as sources) and γ_{45} component tests are

Table 3
Properties of our Seven Lens Samples Binned by Stellar Mass

Sample	$\log(M_*)$	$N_{\rm gal}$	N_{M06}	$\langle z\rangle$	$\sigma(z)$	$\langle\log(M_*)\rangle$
sm1	[9.38, 9.69]	35,269	23,474	0.029	0.007	9.55
sm2	[9.69, 9.99]	62,742	40,952	0.044	0.012	9.85
sm3	[9.99, 10.29]	107,707	66,503	0.069	0.020	10.15
sm4	[10.29, 10.59]	153,787	90,019	0.103	0.030	10.45
sm5	[10.59, 10.89]	155,242	82,734	0.140	0.038	10.73
sm6	[10.89, 11.20]	73,048	39,729	0.150	0.037	11.01
sm7	[11.20, 11.50]	9807	8096	0.150	0.037	11.29

Note. We compare the number of galaxies we use, $N_{\rm gal}$, to the one in Mandelbaum et al. (2006). M_* is in units of $h^{-2}\,M_\odot$.

Table 4
Subsamples Binned in Stellar Mass and Split into Red and Blue

Sample	$N_{\rm gal}$	$\langle z\rangle$	$\sigma(z)$	$\langle\log(M_*)\rangle$
sm1r	7447	0.038	0.010	9.56
sm1b	27,522	0.054	0.016	9.55
sm2r	19,604	0.051	0.015	9.87
sm2b	43,138	0.070	0.020	9.85
sm3r	48,669	0.069	0.019	10.16
sm3b	59,038	0.089	0.026	10.15
sm4r	85,839	0.090	0.025	10.45
sm4b	67,948	0.113	0.032	10.44
sm5r	102,360	0.120	0.036	10.74
sm5b	52,882	0.136	0.037	10.72
sm6r	57,063	0.149	0.037	11.01
sm6b	15,985	0.146	0.038	10.99
sm7r	8224	0.158	0.034	11.29

Note. M_* is in units of $h^{-2}\,M_\odot$.

Table 5
Subsamples Binned in Stellar Mass and Split into Star-forming Galaxies and Quenched Galaxies

Sample	$N_{\rm gal}$	$\langle z\rangle$	$\sigma(z)$	$\langle\log(M_*)\rangle$
sm1sf	29,460	0.053	0.016	9.55
sm1qu	5809	0.038	0.011	9.56
sm2sf	46,544	0.068	0.020	9.85
sm2qu	16,198	0.051	0.016	9.87
sm3sf	66,138	0.086	0.027	10.15
sm3qu	41,569	0.069	0.019	10.16
sm4sf	73,606	0.109	0.031	10.44
sm4qu	80,181	0.090	0.026	10.45
sm5sf	50,107	0.137	0.034	10.72
sm5qu	105,135	0.119	0.034	10.74
sm6sf	11,151	0.157	0.033	10.98
sm6qu	61,897	0.147	0.038	11.01
sm7qu	8219	0.157	0.034	11.29

Note. M_* is in units of $h^{-2}\,M_\odot$.

consistent with zero. Note that these possible systematic errors are mainly associated with the type of source galaxies that are used, where a brighter magnitude cut will reduce the systematics significantly. On the other hand, the total number of galaxies that are used in our investigation impacts the statistical errors. As one can see in Figure 8 below, our results are in good agreement with M05, but with much smaller error bars, since we have a larger number of lens galaxies in our SDSS DR7 galaxy samples. There is a clear trend that the amplitude of $\Delta\Sigma$ increases as the luminosity increases.

Table 6
Five Major Systematics in Our Weak-lensing Measurements Compared to M05

Bias (percent)	M05	This Work
Selection bias	[0, 10.3]	[0, 12.3]
PSF reconstruction bias	±2.1 to ±2.4	±2.2
PSF dilution bias	[−2.8, 4.0]	*[−2.8, 4.0]
Shear responsivity error	[0, 1.7]	[0, 2.3]
Noise rectification error	[−3.8, 0]	[−4.08, 0]
Total 2σ $\delta\gamma/\gamma$(percent)	[−9.0, 18.4]	[−9.1, 20.8]

5.1. Systematic Errors

There are five major systematics in weak-lensing measurements as described in HS03 and M05. Table 6 lists these major biases in our work and compares them to M05. We give below a brief introduction for each of them.

5.1.1. Selection Bias

The first selection bias is mainly caused by the asymmetries of the PSF, denoted as "PSF selection bias" in Kaiser (2000). More galaxies are selected if they are elongated in one direction. Second, the shear introduces asymmetries in the same way as the PSF. Shear stretches galaxies along a certain direction and hence makes the major axes of galaxies aligned with that direction more easily detected. In HS03, this is referred to as the "shear selection bias." Finally, many significance-based object detection methods preferentially select circular objects, leading to underestimation of the shear signal. M05 estimates the selection bias to be [0%, 5.7%] for galaxies with $r < 21$, [0%, 10.3%] for $r > 21$ and [0%, 11.1%] for LRG samples. Both M05 and this work directly use the catalog from the Photo pipeline, and the selection biases from M05 and our catalog will not differ from each other significantly. Following Equation (19) in M05, the selection bias is calculated as

$$\frac{\delta\gamma}{\gamma} = \frac{\bar{R}_{\rm min}(1-\bar{R}_{\rm min})}{\bar{R}} e^2_{\rm rms} n(\bar{R}_{\rm min}), \quad (31)$$

where $\bar{R}$ is the shear responsivity and $n(\bar{R}_{\rm min}) = 1.6$, 2.4, and 2.8 for $r < 21$, $r > 21$, and LRG samples in M05, respectively. We have used the value for $r > 21$ here, estimating $n(\bar{R}_{\rm min})$ for our sample to be 2.4. The maximum possible systematics that can be induced by selection bias is 12.3% in our sample, slightly larger than those obtained by M05.

5.1.2. PSF Reconstruction Bias

This bias arises from the process of reconstructing the PSF from the Photo PSF pipeline. This bias estimated in M05 is

±2.1 to ±2.5 for the SDSS sample. Since the PSFs applied in M05 and this work are both from the Photo PSF pipeline, we follow M05 and also use Equation (20) in Hirata et al. (2004) to estimate this bias,

$$\frac{\delta\gamma}{\gamma} = (\mathcal{R}^{-1} - 1)\frac{\delta T^p}{T^p}. \quad (32)$$

As in H04, we fix $\delta T^p/T^p$ to be 0.03. Due to the fact that the PSF reconstruction pipeline and the PSF size are fixed, T varies very little. The estimated bias is ±2.2%. That is consistent with M05 at ±2.1% for $r < 21$ and ±2.4% for $r > 21$. Our estimate is between these two values because we calculate the bias using all the galaxies with r-band model magnitude.

5.1.3. PSF Dilution Bias

The PSF blurs the image owing to the convolution, which is a function of resolution $\mathcal{R}$ and brightness distribution. An empirical formula of this bias from an ensemble of exponential and de Vaucouleurs distributions is given in M05 as a function of the fraction of the exponential part and the fraction of the de Vaucouleurs part,

$$\frac{\delta\gamma}{\gamma} \geqslant -0.014 f_{\rm exp} - 0.035 f_{\rm deV}. \quad (33)$$

Roughly, this value ranges from −2.8% to 3.9%. As both studies use the Photo PSF pipeline, and because this bias is estimated in a model-dependent method, we directly use M05's estimation as shown in Table 2 (the asterisk indicates that we directly use M05's results).

5.1.4. Shear Responsivity Error

The responsivity $\bar{R}$ is calculated from the variance of ellipticity, indicating that this is related to the ellipticity distribution. Once we use the cut $\mathcal{R} > 1/3$, the distribution has been changed and an error on $\bar{R}$ appears. It ranges from 0% to 1.7% in M05. Our bias estimation using Equation (25) in H04 is 2.3%, with a fixed $\delta e_{\rm rms} = 0.02$ as in H04.

5.1.5. Noise Rectification Bias

This noise, ranging from −3.8% to 0%, is caused by the image noise as described in HS03 (Equations (26) and (27)). The quantification of this bias is

$$\frac{\delta\gamma}{\gamma} \approx K v^{-2} = 4(1 - 3\bar{R}_2^{-1} + \bar{R}_2^{-2} + 2e_{\rm rms}^2)v^{-2}, \quad (34)$$

where v is the S/N of the detection over bands $v^{-2} = \frac{2}{v_r^2 + v_i^2}$. Our estimate of K at $\mathcal{R} = 1/3$ is 5.7, bigger than the 5.3 in M05 and 5.1 in H04. So the lower limit of this bias (2σ) in our sample is −4.08% larger than in M05 and H04.

5.2. Systematic Tests on the Lensing Signals

From weak-lensing shear measurements, we can estimate the excess surface density (ESD) of the lens system, which is defined as

$$\Delta\Sigma(R) = \Sigma(\leqslant R) - \Sigma(R). \quad (35)$$

Here $\Sigma(\leqslant R)$ and $\Sigma(R)$ are the mean surface mass density inside a certain radius R and at the radius R, respectively. The tangential shear is related to this quantity via a critical density,

$$\gamma_t(R)\Sigma_c = \Delta\Sigma(R), \quad (36)$$

where the critical density in a lensing system is

$$\Sigma_c^{-1} = \frac{4\pi G}{c^2}\frac{D_l D_{ls}(1 + z_l)^2}{D_s}, \quad (37)$$

with D_s, D_l, and D_{ls} being the angular diameter distances of the source, the lens, and between the lens and the source, respectively.

The mean ESD around a lens galaxy is related to the line-of-sight projection of the galaxy–matter cross-correlation function,

$$\xi_{\rm gm}(r) = \langle \delta(\boldsymbol{x})_g \delta(\boldsymbol{x} + \boldsymbol{r})_m \rangle, \quad (38)$$

so that

$$\Sigma(R) = 2\overline{\rho}\int_R^\infty \xi_{\rm gm}(r)\frac{r\,dr}{\sqrt{r^2 - R^2}} \quad (39)$$

and

$$\Sigma(\leqslant R) = \frac{4\overline{\rho}}{R^2}\int_0^R y\,dy \int_y^\infty \xi_{\rm gm}(r)\frac{r\,dr}{\sqrt{r^2 - y^2}}, \quad (40)$$

where $\overline{\rho}$ is the average background density of the universe. Note that in both equations we have omitted the contribution from the mean density of the universe, as it does not contribute to the ESD.

In order to take into account source galaxy photometric redshift errors, it is necessary to convolve the results with the error distribution (see M05),

$$\Sigma_c^{-1}(z_l, z_p) = \int p(z_s|z_p)\Sigma_c^{-1}(z_l, z_s)dz_s, \quad (41)$$

where z_l, z_p, z_s are the spectroscopic redshift of the lens galaxy, the photometric redshift of the source galaxy, and the spectroscopic redshift of the source galaxy, respectively. Since the spectroscopic redshifts are not available for most source galaxies, the determination of $p(z_s|z_p)$ relies on other spectroscopic surveys. We follow M05 and use the error distribution obtained by cross-identifying the subsample of their source galaxies with other spectroscopic surveys such as DEEP2 and COMBO-17.

In order to observationally estimate the systematics, three additional tests were carried out: a redshift test, a random sample test, and a 45° rotation test. Any systematics will cause a deviation from the expected zero. Here, for simplicity, we only show results for lens galaxies in different luminosity bins.

5.2.1. Redshift Test

The redshift test is performed first. The lens–source separation used for shear calculation is $z_l < z_s + 0.1$. This criterion has been chosen to avoid cases where the source galaxy may be located in front of the lens galaxy. The value of 0.1 is chosen on the basis that the typical photometric redshift measurement error is 0.025 (Abazajian et al. 2009). If we use $z_l > z_s$, no signal is expected, and a nonzero value would be caused by unknown systematics. Figure 5 shows this systematic test using our SDSS DR7 data. The error bars are estimated using 2500 bootstrap resampling of the lens galaxy samples. The consistency with zero shows that the systematics in our work can be neglected in comparison to the null lensing signals.

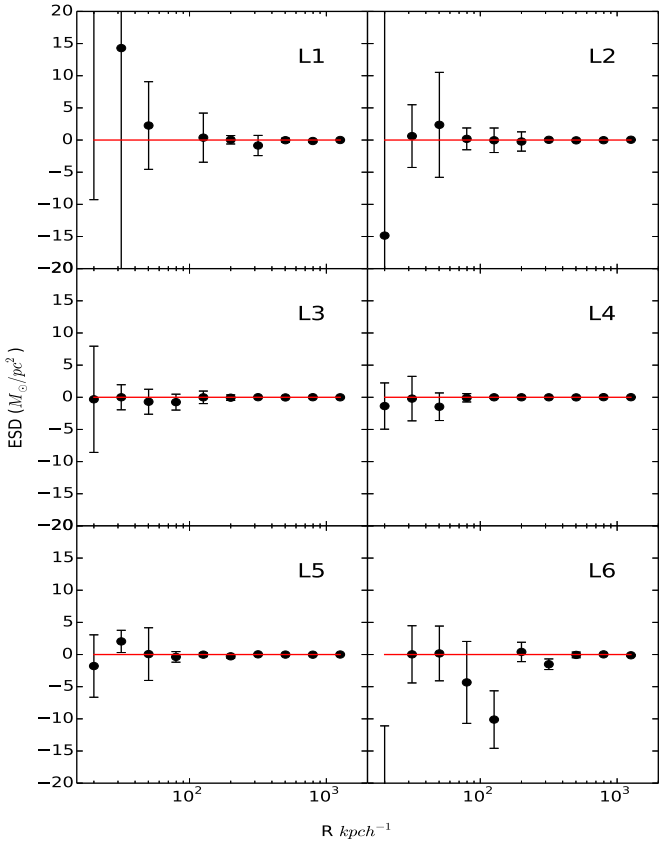

Figure 5. Redshift systematic test. Shown in the plot are the ESDs estimated using sources galaxies that are in front of the lens galaxies.

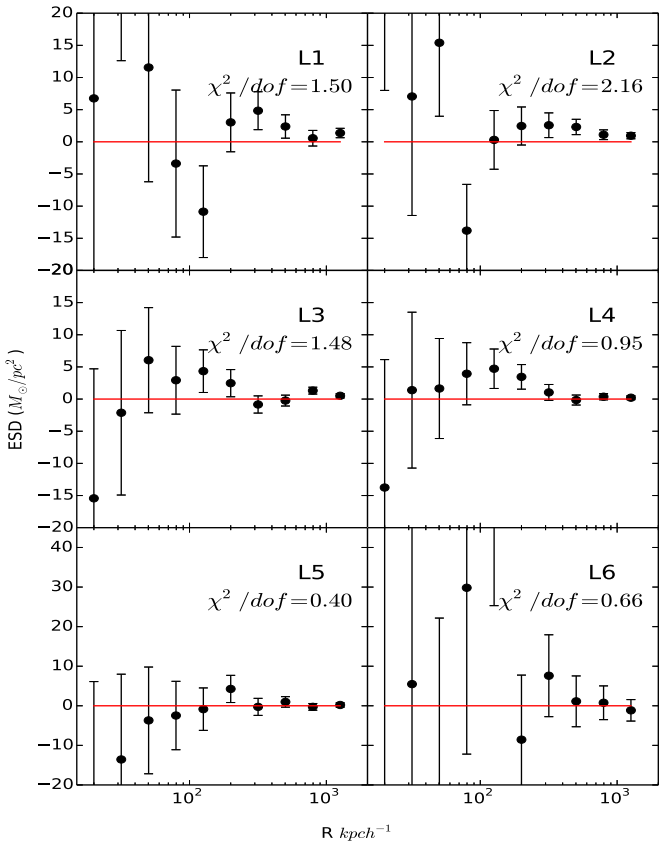

Figure 6. Random sample test, with the ESDs estimated around random lens galaxies.

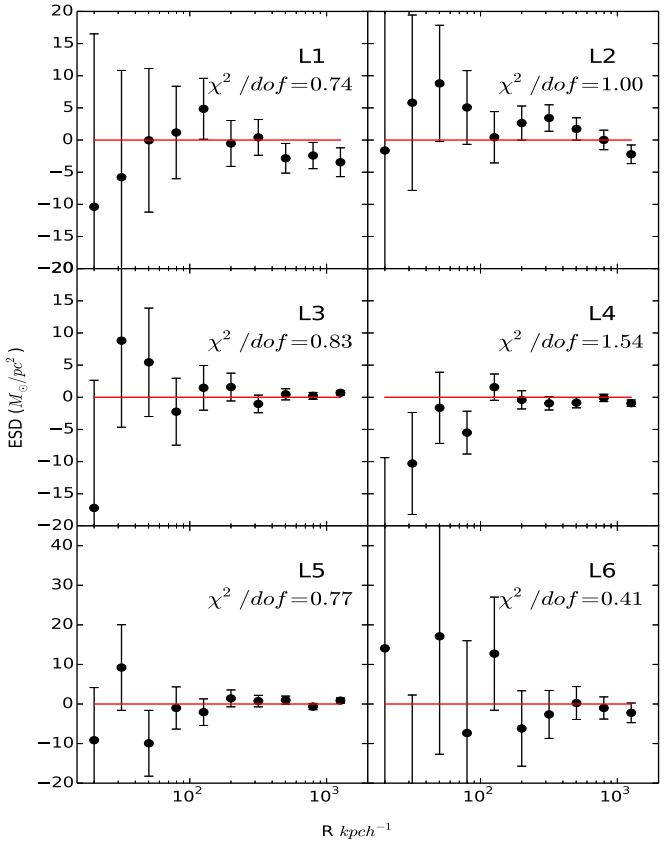

Figure 7. 45° test, with the B-mode ESDs estimated around lens galaxies.

5.2.2. Random Sample Test

For this test, we have used the random catalog constructed in Yang et al. (2012), which was used to calculate the two-point correlation function. This random sample includes all the observational effects from SDSS DR7, i.e., the same luminosity function, magnitude limit, redshift completeness, and sky coverage due to SDSS mask (MANGLE by Hamilton & Tegmark 2004). The total number of random galaxies in the sample is 736,812, slightly larger than the original sample we used. We binned the random sample into the same six luminosity ranges and measured the GG lensing signals around the random samples. Figure 6 shows the signals obtained around the random samples. To access the deviation of the signals from the null hypothesis, we provide the reduced χ^2 value of our signals from zero in each panel. Here the full covariance matrix is used to estimate the χ^2 values. In the three low-luminosity bins, we do see some spurious power at small scales. As pointed out in Mandelbaum et al. (2005), this spurious power was probably caused by the charge transfer efficiency and the SDSS TDI survey pattern.

5.2.3. 45° Rotation Test

Finally, we calculate the B-mode signal using the galaxies in different luminosity bins. Theoretically, weak lensing only introduces tangential distortion, so any signal from γ_{45^o} indicates various systematics, as stated in M05.

We show in Figure 7 the γ_{45^o} in different luminosity bins. Generally speaking, the signals are consistent with zero except for L4, where the reduced χ^2 value is slightly larger.

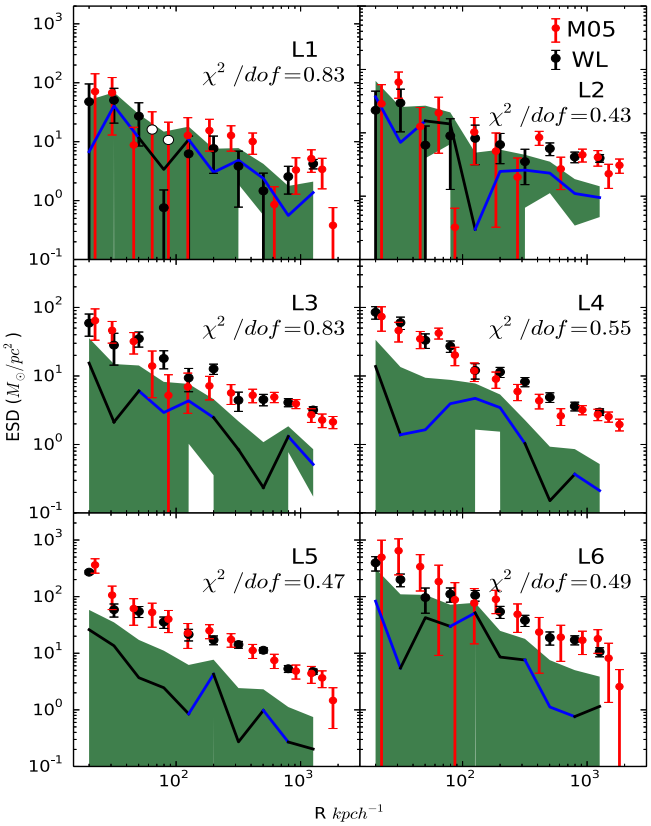

Figure 8. Excess surface density (ESD) of our lens galaxies in six luminosity bins. The black dots are our measurements, and the red dots are results obtained by M05 (with open circles representing the absolute values of the negative data points). The solid line in each panel is the average ESD around random lens galaxies, with blue and black colors for positive and negative values, respectively. The error bars and green shaded regions denote 1σ errors of ESDs estimated using 2500 bootstrap resampling of the lens galaxy samples.

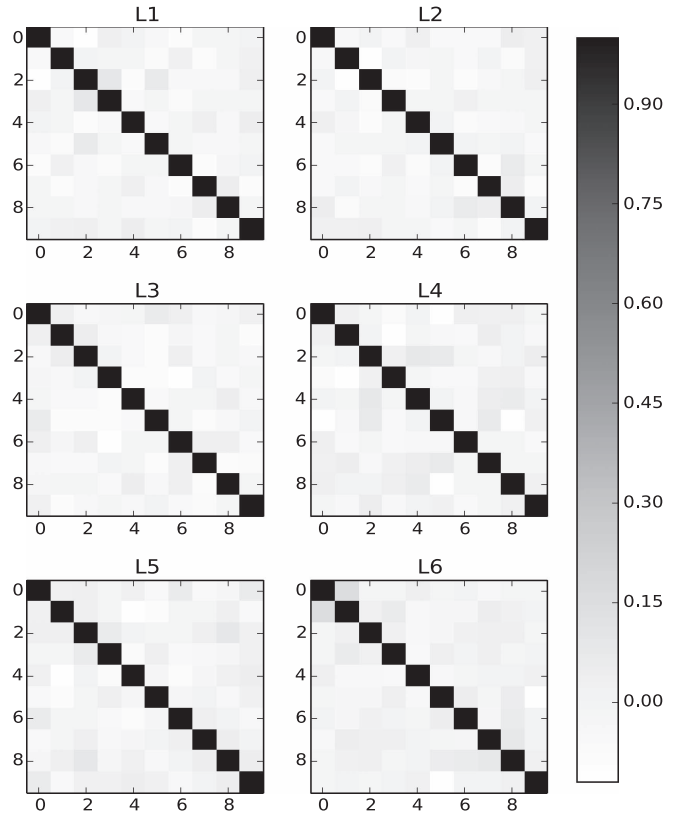

Figure 9. Correlation matrix of the data points for our six luminosity bins. The gray scale has been scaled so that smaller values are reflected on this covariance map. The values of the correlation matrix map are provided in separate files.

6. GG Lensing Signals

With all the above preparations and tests being carried out, we proceed to measure the GG lensing signals in SDSS DR7.

Figure 8 shows the average ESD of our lens galaxies divided into six luminosity bins. The black dots are our measurements, and the red dots show the M05 data (kindly provided by Rachel Mandelbaum). For simplicity, the signals around each galaxy sample were calculated in 10 equal logarithmic bins, rather than 45 bins, and then rebinned as in M05. The error bars are estimated using 2500 bootstrap resampling of the lens galaxy samples. The correlation matrix of the data points shown in Figure 8 is given in Figure 9. We rescaled the color so that smaller values can be seen. Interested readers can find the correlation matrix values via the link provided at the end of Section 1. The ESDs for lens galaxies in different luminosity bins are also listed in Table 7 in Appendix B.

As one can see in Figure 8, there is a clear trend that the amplitude of $\Delta\Sigma$ increases as the luminosity increases. To access the significance of our results, we also plot the ESDs around random lens galaxies using blue (positive value) and black (negative value) solid lines. The 1σ errors are shown as the green shaded regions. We find that the ESD signals for lens galaxies in the two low-luminosity bins barely exceed the random sample values. Thus, our measurements of the ESDs for galaxies are only significant in the four high-luminosity bins. In addition, by comparing to the results obtained by M05, our results show good agreement with M05, with much smaller error bars, since we have a larger number of lens galaxies in our SDSS DR7 galaxy samples. The overall χ^2 values between the two measurements are less than 0.83.

For each of our luminosity bins, we also obtain the GG lensing signals separately for the red and blue subsamples, and the results are presented in Figure 10. The error bars here are larger owing to the decreased number of lens galaxies per subsample. For very faint lens galaxies in the L1 bin, the red galaxies have larger ESDs than blue galaxies, especially at small radius. This indicates that faint red galaxies tend to be located in relatively more massive halos than their blue counterparts. For brighter galaxies, especially in L2–L4 bins, the red and blue galaxies show similar ESDs at small scales (with the caveat that the error bars are big), but red galaxies have much higher amplitudes than their blue counterparts at $R > 200\,h^{-1}$ kpc. The latter indicates that these red galaxies are preferentially located in high-density regions.

We have also estimated the ESDs for galaxies in different stellar mass bins, and the results are shown in Figure 11 with black dots, in comparison with the results of M05, which are shown as the red dots. Here our results show similar trends to those of M06. The reduced χ^2 between the two measurements ranges from 0.60 to 1.87. Discrepancies are seen, especially in the sm5 bin, where our results at $200 < R < 1,500\,h^{-1}$ kpc are significantly (by a factor of about two) higher. There are

Table 7
ESDs of Lens Galaxies That Are Separated into Different Luminosity Bins

R (Mpc/hr)	L1	L2	L3	L4	L5	L6
0.020	47.753 ± 51.318	22.722 ± 31.109	59.068 ± 21.041	85.001 ± 17.596	270.283 ± 19.675	395.426 ± 112.376
0.032	50.609 ± 29.971	29.589 ± 19.232	28.174 ± 13.808	59.956 ± 12.268	58.845 ± 15.307	199.987 ± 50.518
0.050	27.104 ± 18.650	6.401 ± 12.476	35.059 ± 8.693	33.181 ± 7.948	54.852 ± 12.084	96.381 ± 45.461
0.080	0.760 ± 11.775	8.969 ± 7.692	18.018 ± 5.313	27.231 ± 5.129	35.538 ± 8.089	111.051 ± 31.248
0.126	6.225 ± 7.465	8.183 ± 5.040	9.380 ± 3.491	12.053 ± 3.055	21.476 ± 4.981	105.765 ± 22.670
0.200	7.674 ± 4.772	6.517 ± 3.260	12.707 ± 2.162	11.417 ± 1.920	17.160 ± 3.042	54.225 ± 13.056
0.317	3.839 ± 3.063	3.512 ± 1.990	4.422 ± 1.381	8.229 ± 1.269	14.231 ± 1.957	38.240 ± 8.547
0.502	1.463 ± 1.929	5.645 ± 1.282	4.528 ± 0.860	4.891 ± 0.783	11.296 ± 1.183	18.851 ± 4.931
0.796	2.557 ± 1.266	4.166 ± 0.797	4.106 ± 0.551	3.616 ± 0.526	5.322 ± 0.758	17.179 ± 3.135
1.261	4.227 ± 0.773	3.990 ± 0.561	3.191 ± 0.358	2.979 ± 0.333	4.735 ± 0.499	10.577 ± 1.931

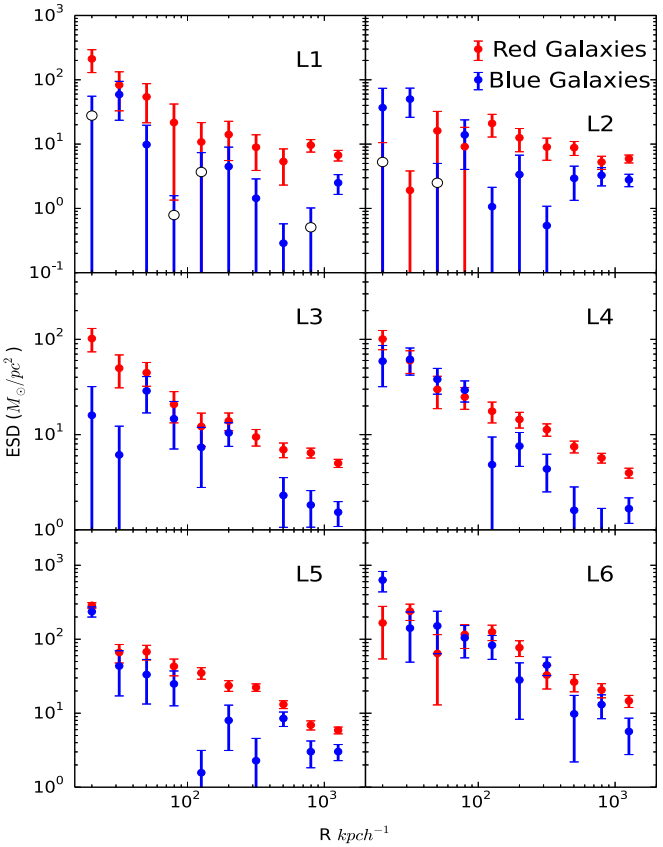

Figure 10. ESDs for red (red dots) and blue (blue dots) galaxies in different luminosity bins. Open dots denote the absolute values of the negative data points.

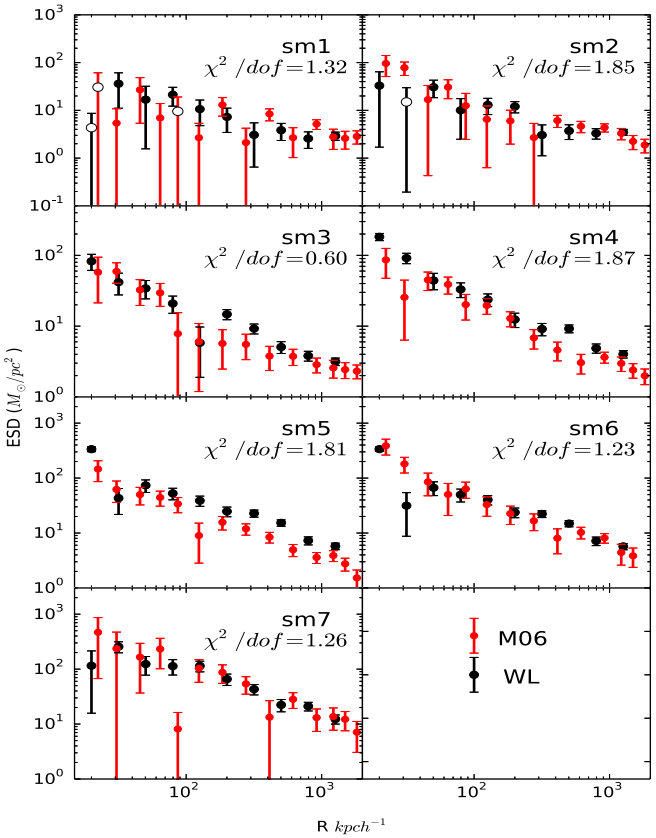

Figure 11. ESDs for lens galaxies of different stellar masses. In each panel we compare our results (black dots) with those of M06 (red dots). Open dots denote the absolute values of the negative data points.

two possible causes of the discrepancies: (i) we used different stellar mass estimators from M06, and (ii) our sample is larger than that of M06 (SDSS DR7 versus DR4). The enhancement in the sm5 bin at $200 < R < 1500\,h^{-1}$ kpc may indicate that a significant portion of the additional galaxies in our sample may be located in or near massive structures. Once again, we provide the ESDs for lens galaxies in different stellar mass bins in Table 8 in Appendix B.

Finally, we also measure the ESDs for our star formation subsamples of color and of star formation in stellar mass bins. Figure 12 shows the results for red versus blue galaxies. The color dependencies in different stellar mass bins are quite similar to those in different luminosity bins. In addition, as the color of a galaxy may be related to the star formation history of the galaxy, the dependence on star formation shown in Figure 13 is similar to the color dependence.

The GG lensing signals can be fitted to obtain the average halo mass of the lens systems. With the results we obtained here, we will be able to study how galaxies of different properties (luminosity, stellar mass, color, and star formation) are linked to dark matter halos. However, as pointed out in Yang et al. (2006a) and found in Li et al. (2014) and Li et al. (2016), the central and satellite galaxies have very different lensing signals. It is thus important to separate samples into centrals and satellites

Table 8
ESDs of Lens Galaxies That Are Separated into Different Stellar Mass Bins

R (Mpc/hr)	sm1	sm2	sm3	sm4	sm5	sm6	sm7
0.020	−4.333 ± 37.732	32.952 ± 31.256	82.383 ± 21.056	182.637 ± 21.271	335.980 ± 33.494	336.404 ± 30.651	115.285 ± 99.517
0.032	36.117 ± 25.027	−14.994 ± 19.186	41.799 ± 14.208	91.604 ± 15.367	43.176 ± 21.400	31.518 ± 22.789	256.227 ± 58.129
0.050	16.766 ± 15.203	30.626 ± 12.198	34.166 ± 9.904	44.174 ± 11.545	73.646 ± 18.962	66.753 ± 18.781	123.575 ± 45.973
0.080	21.305 ± 9.069	10.033 ± 7.549	20.878 ± 5.701	33.090 ± 7.798	52.717 ± 12.550	49.856 ± 13.153	113.419 ± 35.431
0.126	10.617 ± 5.837	13.010 ± 4.850	5.807 ± 3.915	23.703 ± 4.843	38.787 ± 8.170	40.202 ± 7.755	114.243 ± 25.088
0.200	7.286 ± 3.841	12.030 ± 3.186	14.715 ± 2.401	12.398 ± 2.847	24.732 ± 4.965	23.755 ± 4.770	65.843 ± 15.455
0.317	3.062 ± 2.413	3.039 ± 1.921	9.233 ± 1.482	9.110 ± 1.803	22.772 ± 3.356	22.250 ± 3.147	43.172 ± 9.255
0.502	3.836 ± 1.496	3.722 ± 1.273	5.069 ± 0.965	9.217 ± 1.174	15.316 ± 2.050	14.874 ± 1.904	22.356 ± 5.645
0.796	2.573 ± 0.975	3.312 ± 0.817	3.807 ± 0.605	4.872 ± 0.726	7.290 ± 1.218	7.172 ± 1.273	21.094 ± 3.776
1.262	2.929 ± 0.570	3.503 ± 0.497	3.155 ± 0.383	4.023 ± 0.480	5.760 ± 0.786	5.703 ± 0.749	12.316 ± 2.337

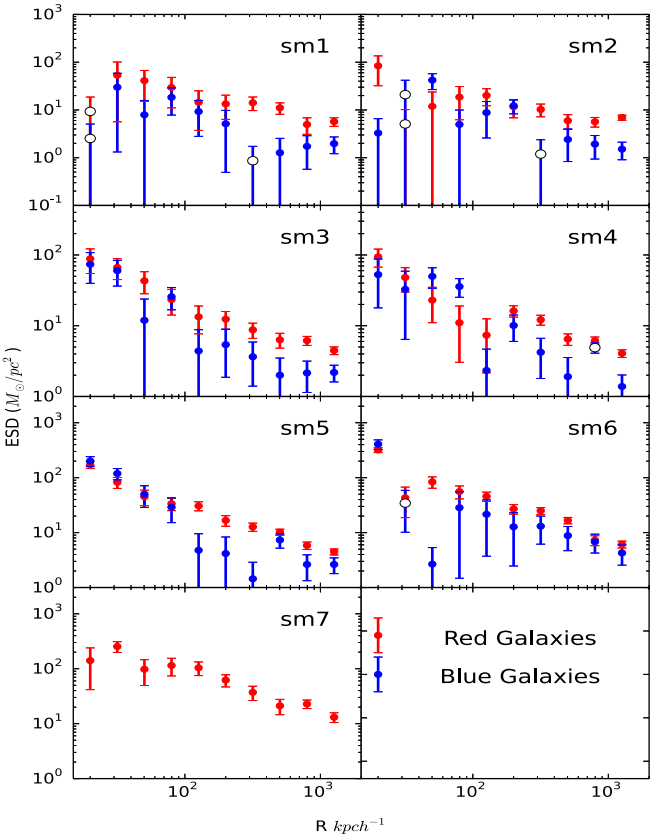

Figure 12. ESDs for red (red dots) and blue (blue dots) lens galaxies in different stellar mass bins. Open dots denote the absolute values of the negative data points.

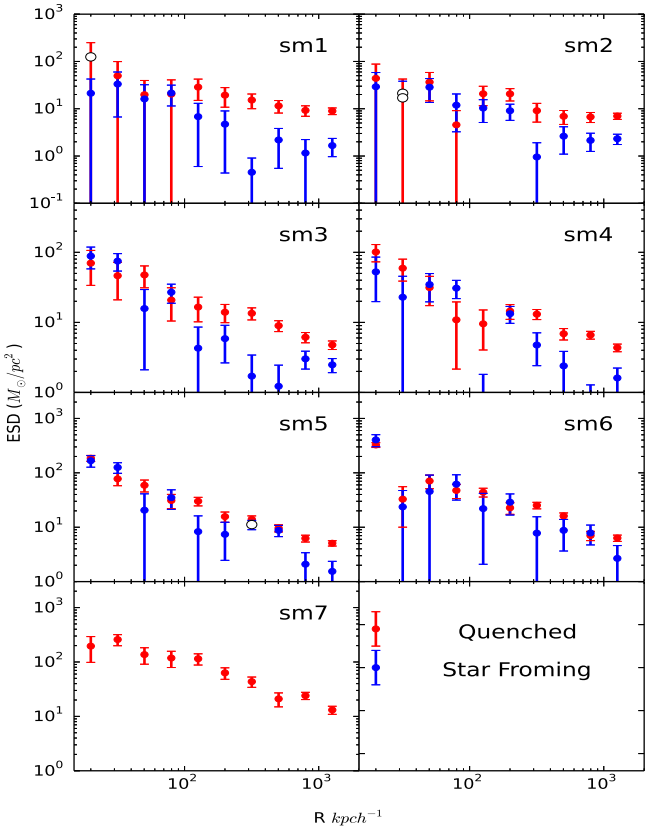

Figure 13. ESDs for quenched (red dots) and star-forming (blue dots) lens galaxies in different stellar mass bins. Open dots denote the absolute values of the negative data points.

in order to model the observed ESDs in detail. We will come back to this in a forthcoming paper.

7. Summary and Discussion

In weak-lensing studies, obtaining a reliable measurement of the lensing signals requires highly accurate image processing. In this paper, we build our image processing pipeline to achieve accurate shape measurement for weak-lensing studies based on the methods of Bernstein & Jarvis (2002, BJ02) and Hirata & Seljak (2003, HS03). This pipeline is then applied to SDSS DR7 to measure the galaxy shapes, as well as the GG lensing signals for lens galaxies of different luminosities, stellar masses, colors, and SFRs. The main results of this paper are summarized as follows:

1. We have developed a new image processing pipeline and tested it on SHERA and GREAT3 simulations. Our pipeline works well on PSF correction in the absence of sky background noise. The corrected PSF multiplicative errors are far below the 1% requirements (0.009% for γ_1 and −0.053% for γ_2) for PSF correction only.
2. A nonconvergence problem occurs for ∼40% of galaxies when more realistic simulations with sky background noise are being used. In addition, to have a sufficient image resolution $\mathcal{R} > 1/3$, an additional 20% have to be

discarded. Despite these, our method achieves a lensing reconstruction accuracy that is similar to other methods as shown in the GREAT3 competition (Mandelbaum et al. 2015).

3. Our pipeline was applied to the SDSS DR7 *r*-band imaging data and created a catalog containing 41,631,361 galaxies with information about position, photometric redshift, ellipticity, and ellipticity measurement error due to sky background and Poisson noise.
4. We have estimated the systematic errors in our shear measurement, which in total are between −9.1% and 20.8% at 2σ levels. In addition, we have performed a number of tests on possible systematics in our pipeline, using the γ_{45} component, foreground sources, and random samples. Our pipeline and the GG lensing signals obtained prove to be reliable against these tests.
5. Using the SDSS DR7 galaxy images, we calculated the GG lensing signals around foreground lens galaxies binned in different luminosities and stellar masses. Our results show good and fair agreement with the previous studies of Mandelbaum et al. (2005, M05) and Mandelbaum et al. (2006, M06), respectively, with significantly reduced error bars.
6. We have also separated the galaxies in different luminosity/stellar mass bins into red/blue or star-forming/quenched subsamples. The GG lensing signals show quite different scale dependences among these subsamples. While red and quenched galaxies show stronger GG lensing signals than their counterparts in the same luminosity or stellar mass bins, the enhancement is the strongest at relatively large separations.

Our data can be used to study the dark matter contents associated with SDSS galaxies and the structures they represent. In a forthcoming paper, we will use the data to carry out a number of analyses. We will separate galaxies into centrals and satellites so as to model the mass distributions around them and their links to dark matter halos. We will also obtain the mass distribution around galaxy groups (Yang et al. 2007) to test the reliability of the mass assignments based on other mass estimates and to study how halo masses depend on the intrinsic properties of galaxy groups, such as the colors of members of galaxy groups. Finally, we will stack the lensing signals around groups with different X-ray properties (e.g., Wang et al. 2014) to test how X-ray gas in galaxy groups is related to their dark matter contents.

As we have found, our pipeline is unable to fully deal with images that are noisy. This limitation is the main drawback of our pipeline and needs to be addressed. Fourier-space-based methods seem to be superior in this regard as they can process asymmetric systems and much noisier images. For this reason, we intend to improve our methodology by implementing the Fourier space method of Zhang et al. (2015).

We thank the anonymous referee for helpful comments that greatly improved the presentation of this paper. W.L. thanks Rachel Mandelbaum from Carnegie Mellon University for very useful guidance and discussions at various stages of this project and for providing the data points presented in this paper. W.L. also thanks Dandan Xu from Heidelberg University for useful discussions. This work was supported by the following programs: the 973 Program (no. 2015CB857002), NSFC (nos. 11128306, 11121062, 11233005, 11503064), the Strategic Priority Research Program "The Emergence of Cosmological Structures" of the Chinese Academy of Sciences, grant no. XDB09000000, and a key laboratory grant from the Office of Science and Technology, Shanghai Municipal Government (no. 11DZ2260700), as well as the Chinese Scholarship Council (no. 201504910477) and Shanghai Natural Science Foundation, grant no. 15ZR1446700. L.F. acknowledges the support from NSFC grant nos. 11333001 and 11673018, STCSM grant nos. 13JC1404400 and 16R1424800, and SHNU grant no. DYL201603. F.C.v.d.B. is supported by the Klaus Tschira Foundation and by the U.S. National Science Foundation through grant AST 1516962. L.R. acknowledges the NSFC (grant no.11303033) and the support from the Youth Innovation Promotion Association of CAS.

This work was also supported by the High Performance Computing Resource in the Core Facility for Advanced Research Computing at Shanghai Astronomical Observatory.

Appendix A
BJ02 Method

We use this first appendix to detail the mathematical derivation of the PSF anisotropy correction of the pipeline presented in this paper. We follow BJ02 using the following eigenfunction expansion for our images:

$$K = \sum_{kl} k_{kl} D_{kl}, \tag{42}$$

where

$$\begin{aligned} D_{kl} &= \left(\frac{\partial}{\partial x} + i\frac{\partial}{\partial y}\right)^k \left(\frac{\partial}{\partial x} - i\frac{\partial}{\partial y}\right)^l \\ &= \sigma^{-(k+l)} (a_q^{\sigma\downarrow} - a_p^{\sigma\uparrow})^k (a_p^{\sigma\downarrow} - a_q^{\sigma\uparrow})^l. \end{aligned} \tag{43}$$

Note that k, l in D_{kl} are the index of matrix components, while on the right-hand sides they represent power indices. The operators $a_p^{\downarrow}$ and $a_p^{\uparrow}$ are the lowering and raising operators for the 2D QHO eigenfunctions, respectively, which have the properties that

$$\begin{aligned} a_p^{\downarrow} &= \frac{1}{2}\left[\frac{x - iy}{\sigma} + \sigma\left(\frac{\partial}{\partial x} - i\frac{\partial}{\partial y}\right)\right], \\ a_p^{\uparrow} &= \frac{1}{2}\left[\frac{x + iy}{\sigma} - \sigma\left(\frac{\partial}{\partial x} + i\frac{\partial}{\partial y}\right)\right], \\ a_q^{\downarrow} &= \frac{1}{2}\left[\frac{x + iy}{\sigma} + \sigma\left(\frac{\partial}{\partial x} + i\frac{\partial}{\partial y}\right)\right], \\ a_q^{\uparrow} &= \frac{1}{2}\left[\frac{x - iy}{\sigma} - \sigma\left(\frac{\partial}{\partial x} - i\frac{\partial}{\partial y}\right)\right]. \end{aligned} \tag{44}$$

The matrix D_{kl} defined above makes it easy to use the raising and lowering operators to determine how a given kernel will act on an image. As we are dealing with discrete image data, the derivative along the x- and y-axes can be treated as convolving

a 3×3 matrix with the image $I(x, y)$,

$$\frac{\partial I}{\partial x} = \begin{pmatrix} 0 & 0 & 0 \\ \frac{-1}{2} & 0 & \frac{1}{2} \\ 0 & 0 & 0 \end{pmatrix} \otimes I,$$

$$\frac{\partial I}{\partial y} = \begin{pmatrix} 0 & \frac{1}{2} & 0 \\ 0 & 0 & 0 \\ 0 & \frac{-1}{2} & 0 \end{pmatrix} \otimes I,$$

$$\frac{\partial^2 I}{\partial x^2} = \begin{pmatrix} 0 & 0 & 0 \\ 1 & -2 & 1 \\ 0 & 0 & 0 \end{pmatrix} \otimes I,$$

$$\frac{\partial^2 I}{\partial y^2} = \begin{pmatrix} 0 & 1 & 0 \\ 0 & -2 & 0 \\ 0 & 1 & 0 \end{pmatrix} \otimes I,$$

$$\frac{\partial^2 I}{\partial x \partial y} = \begin{pmatrix} \frac{-1}{4} & 0 & \frac{1}{4} \\ 0 & 0 & 0 \\ \frac{1}{4} & 0 & \frac{-1}{4} \end{pmatrix} \otimes I. \quad (45)$$

These are all the components up to the second derivative in the gradient direction one can get from the 3×3 discrete image pixels. The related D_{kl} in Equation (43) are

$$D_{10} = \begin{pmatrix} 0 & i(1/2) & 0 \\ -1/2 & 0 & 1/2 \\ 0 & i(-1/2) & 0 \end{pmatrix}; D_{01} = \overline{D_{10}}, \quad (46)$$

$$D_{20} = \begin{pmatrix} i(-1/2) & -1 & i(1/2) \\ 1 & 0 & 1 \\ i(1/2) & -1 & i(-1/2) \end{pmatrix}; D_{02} = \overline{D_{20}}, \quad (47)$$

$$D_{11} = \begin{pmatrix} 0 & 1 & 0 \\ 1 & -4 & 1 \\ 0 & 1 & 0 \end{pmatrix}, \quad (48)$$

$$D_{10} = \begin{pmatrix} 0 & i(1/2) & 0 \\ -1/2 & 0 & 1/2 \\ 0 & i(-1/2) & 0 \end{pmatrix} = \overline{D_{01}},$$

$$D_{20} = \begin{pmatrix} i(-1/2) & -1 & i(1/2) \\ 1 & 0 & 1 \\ i(1/2) & -1 & i(-1/2) \end{pmatrix} = \overline{D_{02}},$$

$$D_{11} = \begin{pmatrix} 0 & 1 & 0 \\ 1 & -4 & 1 \\ 0 & 1 & 0 \end{pmatrix}. \quad (49)$$

Note that D_{00} is the identical matrix, and D_{11} is actually a Laplacian operator. The components listed above contain all the first- and second-order derivatives. Higher-order derivatives can be obtained by convolving the above 3×3 components. For instance, $D_{22} = D_{20} \otimes D_{02}$. Note that since D_{ij} are complex, to end up as a real image, k_{ij} are required to satisfy $k_{ij} = \overline{k_{ij}}$.

Combining Equations (8) and (42), we have

$$b^* = \sum_{ij} k_{ij} D_{ij} b, \quad (50)$$

where $D_{ij}b$ obeys the recursion:

$$D_{00}b = b,$$
$$D_{(i+1)j}b = \frac{1}{\sigma}(a_q^{\downarrow} - a_p^{\uparrow}) D_{ij} b,$$
$$D_{i(j+1)}b = \frac{1}{\sigma}(a_p^{\downarrow} - a_q^{\uparrow}) D_{ij} b. \quad (51)$$

The final step is to constrain the coefficients k_{ij} by requiring b^* to meet the requirements

$$b^*_{pq} = 0, (m = p - q = 2). \quad (52)$$

We construct a 5×5 kernel to remove the anisotropy. For simplicity, however, we demonstrate the procedure by reconstructing a 3×3 kernel to an upper limit $p + q \leqslant N = 4$. Increasing to higher-order expansion does not improve our results significantly. The coefficient matrix used to constrain k_{ij} is then

$$b^* = \begin{pmatrix} b^*_{00} & b^*_{01} & b^*_{02} \\ b^*_{10} & b^*_{11} & b^*_{12} \\ b^*_{20} & b^*_{21} & b^*_{22} \end{pmatrix}. \quad (53)$$

In the ideal case, we have

$$b^* = \begin{pmatrix} \frac{1}{\sqrt{\pi}} & 0 & 0 \\ 0 & -\frac{1}{\sqrt{\pi}} & 0 \\ 0 & 0 & \frac{1}{\sqrt{\pi}} \end{pmatrix}. \quad (54)$$

Since b^*_{10} naturally goes to zero if the PSF's centroid is measured accurately, this term does not have any constraining power on k_{ij}. For the unspecified b^*_{pq}, e.g., b^*_{31}, b^*_{40}, we set $k_{pq} = 0$ as in BJ02 while still meeting the kernel requirement to remove the PSF anisotropy to some order. The components that remain are only b^*_{00}, b^*_{11}, b^*_{20}, and b^*_{22}. The linear equation to calculate k_{ij} is then

$$\begin{pmatrix} D_{00}b_{00} & D_{01}b_{00} & D_{02}b_{00} & D_{11}b_{00} \\ D_{00}b_{11} & D_{01}b_{11} & D_{02}b_{11} & D_{11}b_{11} \\ D_{00}b_{11} & D_{01}b_{20} & D_{02}b_{20} & D_{11}b_{20} \\ D_{00}b_{22} & D_{01}b_{22} & D_{02}b_{22} & D_{11}b_{22} \end{pmatrix} \begin{pmatrix} k_{00} \\ k_{10} \\ k_{02} \\ k_{11} \end{pmatrix}$$
$$= \begin{pmatrix} b^*_{00} \\ b^*_{11} \\ b^*_{20} \\ b^*_{22} \end{pmatrix} = \begin{pmatrix} \frac{1}{\sqrt{\pi}} \\ -\frac{1}{\sqrt{\pi}} \\ 0 \\ \frac{1}{\sqrt{\pi}} \end{pmatrix}. \quad (55)$$

Owing to the fact that $k_{kl} = \bar{k_{kl}}$, the dimensions shrink dramatically while considering k_{01} and k_{02}. Before solving this linear equation, we have to calculate each element of the coefficient matrix. $D_{kl}\boldsymbol{b}$ denotes all the entries of the coefficient vector when expanding the PSF image using elliptical Laguerre polynomials. In practice, for the pixelized image data, $D_{kl}\boldsymbol{b}$ can

be written as follows:

$$D_{10}\boldsymbol{b} = \frac{1}{2}(T_{z1}\boldsymbol{b} - T_{-z1}\boldsymbol{b}) + \frac{1}{2}i(T_{z2}\boldsymbol{b} - T_{-z2}\boldsymbol{b}), \quad (56)$$

where $z1 = 1/\sigma$ and $z2 = i/\sigma$. T_z is defined as the translation operator,

$$T_z f(x, y) = f(x - x_0, y - y_0), \quad z = (x_0 + iy_0)/\sigma. \quad (57)$$

Thus, we have

$$T_{z1} f(x, y) = f(x - 1, y), \quad T_{z2} f(x, y) = f(x, y - 1). \quad (58)$$

The functional form of T_z can be derived from the decomposition of the PSF image, i.e., $P = \sum b_{pq}\psi^{\sigma}_{pq}$ and $T_z P = \sum b'_{pq}\psi^{\sigma}_{pq}$. We denote $\boldsymbol{b}'$ as the new coefficients after operation T_z,

$$\begin{aligned} \boldsymbol{b}' &= T_z\boldsymbol{b}, \\ b'_{p'q'} &= \sum T^{pq}_{p'q'} b_{pq}, \\ T_z\psi^{\sigma}_{pq} &= \sum T^{pq}_{p'q'}\psi^{\sigma}_{p'q'}, \\ T^{pq}_{p'q'} &= \sigma^2 \int d^2x (T_z\psi^{\sigma}_{pq})\psi^{\bar{\sigma}}_{p'q'}. \end{aligned} \quad (59)$$

This directly leads to the first term,

$$T^{00}_{00} = e^{-|z|^2/4}. \quad (60)$$

The left-hand terms can also be solved recursively with the following relation:

$$\begin{aligned} T^{pq}_{p'q'} &= h(p, p')\bar{h}(q, q'), \\ h(p, 0) &= \frac{(-z/2)^p}{\sqrt{p!}} e^{-|z|^2/8}, \\ h(p, p' + 1) &= [\sqrt{p}\,h(p - 1, p') \\ &\quad + \frac{1}{2}\bar{z}h(p, p')]/\sqrt{p' + 1}. \end{aligned} \quad (61)$$

Appendix B
The ESDs of Lens Galaxies

In this appendix we provide the ESD measurements for our SDSS DR7 lens samples in different luminosity and stellar mass bins, in Tables 7 and 8, respectively. ESDs for galaxy subsamples separated by color and by SFR, along with *all* the relevant covariance matrices, are provided in electronic files publicly available via the link http://gax.shao.ac.cn/wtluo/weak_lensing/wl_sdss_dr7.tar.

References

Abazajian, K. N., Adelman-McCarthy, J. K., Agüeros, M. A., et al. 2009, ApJS, 182, 543
Bacon, D. J., & Taylor, A. N. 2003, MNRAS, 344, 1307
Bartelmann, M., & Schneider, P. 2001, PhR, 340, 291
Bell, E. F., McIntosh, D. H., Katz, N., & Weinberg, M. D. 2003, ApJS, 149, 289
Bernstein, G. M. 2009, ApJ, 695, 652
Bernstein, G. M., & Armstrong, R. 2014, MNRAS, 438, 1880
Bernstein, G. M., & Jarvis, M. 2002, AJ, 123, 583
Bertin, E., & Arnouts, S. 1996, A&AS, 117, 393
Bertone, G., Hooper, D., & Silk, J. 2005, PhR, 405, 279
Blanton, M. R., Brinkmann, J., Csabai, I., et al. 2003, AJ, 125, 2348
Blanton, M. R., Schlegel, D. J., Strauss, M. A., et al. 2005, AJ, 129, 2562
Bolton, A. S., Burles, S., Koopmans, L. V. E., et al. 2008, ApJ, 682, 964
Bridle, S., Shawe-Taylor, J., Amara, A., et al. 2009, AnApS, 3, 6
Bridle, S. L., Kneib, J.-P., Bardeau, S., & Gull, S. F. 2002, in The Shapes of Galaxies and Their Dark Halos , ed. P. Natarajan (Singapore: World Scientific)
Broadhurst, T., Benítez, N., Coe, D., et al. 2005, ApJ, 621, 53
Cabanac, R. A., Alard, C., Dantel-Fort, M., et al. 2007, A&A, 461, 813
Cacciato, M., van den Bosch, F. C., More, S., et al. 2009, MNRAS, 394, 929
Coe, D., Zitrin, A., Carrasco, M., et al. 2013, ApJ, 762, 32
Dalal, N., Hennawi, J. F., Holder, G., & Bode, P. 2005, in Gravitational Lensing Impact on Cosmology, Vol. 225, ed. Y. Mellier (Cambridge: Cambridge Univ. Press), 193
Feng, J. L. 2010, ARA&A, 48, 495
Fu, L., Semboloni, E., Hoekstra, H., et al. 2008, A&A, 479, 9
George, M. R., Leauthaud, A., Bundy, K., et al. 2012, ApJ, 757, 2
Gunn, J. E., Carr, M., Rockosi, C., et al. 1998, AJ, 116, 3040
Hamilton, A. J. S., & Tegmark, M. 2004, MNRAS, 349, 115
Heymans, C., Brown, M. L., Barden, M., et al. 2005, MNRAS, 361, 160
Heymans, C., Van Waerbeke, L., Bacon, D., et al. 2006, MNRAS, 368, 1323
Heymans, C., Van Waerbeke, L., Miller, L., et al. 2012, MNRAS, 427, 146
Hirata, C., & Seljak, U. 2003, MNRAS, 343, 459
Hirata, C. M., Mandelbaum, R., Seljak, U., et al. 2004, MNRAS, 353, 529
Jarvis, M., Sheldon, E., Zuntz, J., et al. 2015, arXiv:1507.05603
Kaifu, N. 1998, Proc. SPIE, 3352, 14
Kaiser, N. 2000, ApJ, 537, 555
Kaiser, N., Squires, G., & Broadhurst, T. 1995, ApJ, 449, 460
Kauffmann, G., Heckman, T. M., White, S. D. M., et al. 2003, MNRAS, 341, 33
Kilbinger, M., Fu, L., Heymans, C., et al. 2013, MNRAS, 430, 2200
Kitching, T., Balan, S., Bernstein, G., et al. 2010, arXiv:1009.0779
Kitching, T. D., Miller, L., Heymans, C. E., van Waerbeke, L., & Heavens, A. F. 2008, MNRAS, 390, 149
Kneib, J.-P., Ellis, R. S., Santos, M. R., & Richard, J. 2004, ApJ, 607, 697
Koekemoer, A. M., Aussel, H., Calzetti, D., et al. 2007, ApJS, 172, 196
Kuijken, K., Heymans, C., Hildebrandt, H., et al. 2015, MNRAS, 454, 3500
Leauthaud, A., Massey, R., Kneib, J.-P., et al. 2007, ApJS, 172, 219
Li, R., Mo, H. J., Fan, Z., et al. 2009, MNRAS, 394, 1016
Li, R., Mo, H. J., Fan, Z., Yang, X., & Bosch, F. C. v. d. 2013, MNRAS, 430, 3359
Li, R., Shan, H., Kneib, J.-P., et al. 2016, MNRAS, 458, 2573
Li, R., Shan, H., Mo, H., et al. 2014, MNRAS, 438, 2864
Liu, X., Pan, C., Li, R., et al. 2015, MNRAS, 450, 2888
LSST Science Collaboration, Abell, P. A., Allison, J., et al. 2009, arXiv:0912.0201
Luo, W., Yang, X., & Zhang, Y. 2014, ApJL, 789, L16
Lupton, R., Gunn, J. E., Ivezić, Z., Knapp, G. R., & Kent, S. 2001, adass X, 238, 269
Mandelbaum, R., Hirata, C. M., Leauthaud, A., Massey, R. J., & Rhodes, J. 2012, MNRAS, 420, 1518
Mandelbaum, R., Hirata, C. M., Seljak, U., et al. 2005, MNRAS, 361, 1287
Mandelbaum, R., Li, C., Kauffmann, G., & White, S. D. M. 2009a, MNRAS, 393, 377
Mandelbaum, R., Rowe, B., Armstrong, R., et al. 2015, MNRAS, 450, 2963
Mandelbaum, R., Rowe, B., Bosch, J., et al. 2014, ApJS, 212, 5
Mandelbaum, R., Seljak, U., Hirata, C. M., et al. 2008, MNRAS, 386, 781
Mandelbaum, R., Seljak, U., Kauffmann, G., Hirata, C. M., & Brinkmann, J. 2006, MNRAS, 368, 715
Mandelbaum, R., Slosar, A., Baldauf, T., et al. 2013, MNRAS, 432, 1544
Mandelbaum, R., van de Ven, G., & Keeton, C. R. 2009b, MNRAS, 398, 635
Maoli, R., Mellier, Y., van Waerbeke, L., et al. 2000, Msngr, 101, 10
Massey, R., Heymans, C., Bergé, J., et al. 2007a, MNRAS, 376, 13
Massey, R., Stoughton, C., Leauthaud, A., et al. 2010, MNRAS, 401, 371
Miller, L., Heymans, C., Kitching, T. D., et al. 2013, MNRAS, 429, 2858
Miller, L., Kitching, T. D., Heymans, C., Heavens, A. F., & van Waerbeke, L. 2007, MNRAS, 382, 315
Mo, H., van den Bosch, F. C., & White, S. 2010, Galaxy Formation and Evolution (Cambridge: Cambridge Univ. Press)
Oguri, M., Hennawi, J. F., Gladders, M. D., et al. 2009, ApJ, 699, 1038
Oguri, M., Takada, M., Okabe, N., & Smith, G. P. 2010, MNRAS, 405, 2215
Oguri, M., Taruya, A., Suto, Y., & Turner, E. L. 2002, ApJ, 568, 488
Refregier, A. 2003, ARA&A, 41, 645
Refregier, A., Amara, A., Kitching, T. D., et al. 2010, arXiv:1001.0061
Rhodes, J., Refregier, A., & Groth, E. J. 2000, ApJ, 536, 79
Rowe, B. T. P., Jarvis, M., Mandelbaum, R., et al. 2015, A&C, 10, 121

Scoville, N., Abraham, R. G., Aussel, H., et al. 2007a, ApJS, 172, 38
Scoville, N., Aussel, H., Brusa, M., et al. 2007b, ApJS, 172, 1
Sheldon, E. S., Johnston, D. E., Frieman, J. A., et al. 2004, AJ, 127, 2544
Sheldon, E. S., Johnston, D. E., Scranton, R., et al. 2009, ApJ, 703, 2217
Treu, T., Koopmans, L. V., Bolton, A. S., Burles, S., & Moustakas, L. A. 2006, ApJ, 640, 662
Umetsu, K., Takada, M., & Broadhurst, T. 2007, MPLA, 22, 2099
van Waerbeke, L. 2001, in Cosmological Physics with Gravitational Lensing, ed. J. Thanh Van Tran, Y. Mellier, & M. Moniez (Les Ulis: EDP Sciences), 165
Walsh, D., Wills, B. J., & Wills, D. 1979, MNRAS, 189, 667
Wang, L., Yang, X., Shen, S., et al. 2014, MNRAS, 439, 611
Wittman, D., Dell'Antonio, I. P., Hughes, J. P., et al. 2006, ApJ, 643, 128
Yang, X., Mo, H. J., van den Bosch, F. C., et al. 2006a, MNRAS, 373, 1159
Yang, X., Mo, H. J., & van den Bosch, F. C. 2006b, ApJL, 638, L55
Yang, X., Mo, H. J., van den Bosch, F. C., et al. 2007, ApJ, 671, 153
Yang, X., Mo, H. J., & van den Bosch, F. C. 2008, ApJ, 676, 248
Yang, X., Mo, H. J., van den Bosch, F. C., et al. 2013, ApJ, 770, 115
Yang, X., Mo, H. J., van den Bosch, F. C., Zhang, Y., & Han, J. 2012, ApJ, 752, 41
Yang, X. H., Mo, H. J., Kauffmann, G., & Chu, Y. Q. 2003, MNRAS, 339, 387
York, D. G., Adelman, J., Anderson, J. E., Jr., et al. 2000, AJ, 120, 1579
Zhang, J. 2010, MNRAS, 403, 673
Zhang, J. 2011, JCAP, 11, 041
Zhang, J. 2016, National Science Review, 3, 159
Zhang, J., Luo, W., & Foucaud, S. 2015, JCAP, 1, 024